

1 Labrador Sea sub-surface density as a precursor of 2 multi-decadal variability in the North Atlantic: a multi-model 3 study.

4
5 Pablo Ortega^{1,2}, Jon I. Robson¹, Matthew Menary³, Rowan T. Sutton¹, Adam Blaker⁴, Agathe
6 Germe⁴, J el J.-M. Hirschi⁴, Bablu Sinha⁴, Leon Hermanson⁵ and Stephen Yeager⁶

7 ¹NCAS, University of Reading, Reading, UK

8 ²Barcelona Supercomputing Center, Barcelona, Spain

9 ³LOCEAN, Sorbonne Universit s

10 ⁴National Oceanography Centre, European Way, Southampton, SO14 3ZH, UK

11 ⁵Met Office Hadley Centre, Exeter, UK

12 ⁶National Center for Atmospheric Research, Boulder, USA

13 *Correspondence to:* Pablo Ortega (pablo.ortega@bsc.es)

14 **Abstract.** The Subpolar North Atlantic (SPNA) is a region with prominent decadal variability that has experienced
15 remarkable warming and cooling trends in the last few decades. These observed trends have been preceded by
16 slow-paced increases and decreases in the Labrador Sea density (LSD), which are thought to be a precursor of large
17 scale ocean circulation changes. This article analyses the inter-relationships between the LSD and the wider North
18 Atlantic across an ensemble of coupled climate model simulations. In particular, it analyses the link between
19 subsurface density and the deep boundary density, the Atlantic Meridional Overturning Circulation (AMOC), the
20 Subpolar Gyre (SPG) circulation, and the upper ocean temperature in the eastern SPNA.

21
22 All simulations exhibit considerable multidecadal variability in the LSD and the ocean circulation indices, which are
23 found to be interrelated. LSD is strongly linked with the strength of subpolar AMOC and gyre circulation, and is
24 also linked with the subtropical AMOC, although the strength of this relationship is model dependent and affected
25 by the inclusion of the Ekman component. The connectivity of LSD with the subtropics is found to be sensitive to
26 different model features, including: the mean density stratification in the Labrador Sea; the strength and depth of the
27 AMOC; and the depth at which the LSD propagates southward along the western boundary. Several of these
28 quantities can also be computed from observations, and comparison with these observation-based quantities suggests
29 that models representing a weaker link with the subtropical AMOC might be more realistic.

30 1. Introduction

31
32 The North Atlantic Ocean is a key component in Earth's climate through, for example, its role in redistributing heat
33 and in taking up excess heat and carbon from the atmosphere. It is also a region that has varied significantly in the
34 past. This is particularly true for the North Atlantic subpolar gyre, that has varied significantly on multi-decadal
35 timescales across a range of different variables (H kkinen and Rhines, 2004; Holliday et al., 2020; Reverdin, 2010;
36 Robson et al., 2018b). Basin-mean sea surface temperature (SST) over the North Atlantic has also been observed to
37 vary on multi-decadal timescales (Schlesinger and Ramankutty, 1994), and has been linked to a range of important
38 climate impacts, including hurricane numbers and rainfall in monsoon regions (Knight et al., 2006; Monerie et al.,
39 2019; Zhang and Delworth, 2006). The North Atlantic is also expected to change significantly in the future due to

40 the effects of climate change, and consequently produce substantial climate impacts on the surrounding regions
41 (Sutton and Hodson, 2005; Woollings et al., 2012). On decadal timescales, it is the interaction between natural
42 variability and externally forced changes that will shape how the Atlantic regions climate will evolve. Therefore, in
43 order to improve predictions of the North Atlantic, it is imperative that we improve our understanding of the
44 processes that control decadal timescale changes in this region.

45

46 It has generally been thought that changes in the ocean circulation, and particularly the Atlantic Meridional
47 Overturning Circulation (AMOC), have played a significant role in shaping the Atlantic Multidecadal Variability
48 (AMV; Knight et al. 2005). In particular, changes in the strength of the AMOC, and its related ocean heat transports
49 have been shown to control multi-decadal internal variability in a range of coupled climate models (Danabasoglu,
50 2008; Dong and Sutton, 2005; Jungclaus et al., 2005; Ortega et al., 2011, 2015). The proposed mechanisms to
51 explain the multi-decadal variability involve interplays between the North Atlantic Oscillation (NAO), North
52 Atlantic Deep Water (NADW) formation, the boundary currents, the Gulf Stream and gyre circulations, and the
53 horizontal density gradients (e.g. Joyce and Zhang, 2010; Polyakov et al., 2010; Ba et al., 2013; Nigam et al., 2018;
54 Zhang et al., 2019). Changes in AMOC and the wider ocean circulation have been indeed used to explain the
55 observed changes in the subpolar North Atlantic (SPNA) on decadal and longer timescales (Moat et al., 2019). In
56 particular, the SPNA underwent a rapid warming and salinification in the mid 1990s before a decadal timescale
57 cooling and freshening started in 2005, which is consistent with decadal-to-multidecadal variability of the AMOC
58 (Robson et al., 2012, 2013, 2016). The recent cooling has been linked to climate impacts over the continents,
59 including heat waves (Duchez et al., 2016), through an effect on the position on the jet stream (Josey et al., 2018). A
60 long term relative cooling of the SPNA since ~1850 has also been attributed to a centennial weakening of the
61 AMOC (Caesar et al., 2018; Rahmstorf et al., 2015), an AMOC reduction that most CMIP6 model projections
62 predict to continue in the future (Weijer et al., 2020). However, a lack of direct observations of the strength of the
63 AMOC or the ocean circulation more generally have hindered our ability to make a direct attribution of recent
64 changes.

65

66 In order to understand the aforementioned changes in the SPNA on multi-decadal timescales many authors have
67 turned to indirect measurements of the AMOC. One particular proxy of AMOC strength that has received some
68 focus recently are density anomalies at depth in the western SPNA or Labrador Sea region. In climate models,
69 density anomalies in the western SPNA are a key predictor of density anomalies further south on the western
70 boundary, and hence of the AMOC strength via thermal wind balance (Hodson and Sutton, 2012; Ortega et al.,
71 2017; Robson et al., 2014, 2016). Observations show considerable decadal variability in subsurface density
72 anomalies; density anomalies in the western SPNA or Labrador Sea between ~1000-2500 m increased significantly
73 and peaked in ~1995 and subsequently declined (Robson et al., 2016; Yashayaev and Loder, 2016). Therefore, these
74 density anomalies have been interpreted as indicating that the AMOC peaked circa mid-to-late 1990s, and then
75 declined, consistent with the warming and then cooling of the eastern SPNA (Hermanson et al., 2014; Ortega et al.,
76 2017; Robson et al., 2016). Time series of subsurface density anomalies in the western SPNA are also consistent
77 with other proxies of AMOC strength, including sea level based proxies (McCarthy et al., 2015; Sutton et al., 2018),
78 sediment based proxies (Thornalley et al., 2018), and upper ocean heat content fingerprints (Caesar et al., 2018;
79 Zhang, 2008). Furthermore, the decline in AMOC suggested by the above proxies is also consistent with the
80 observed AMOC decline at 26°N since 2004 (Smeed et al., 2018), and also with the changes in AMOC seen in
81 ocean data assimilation systems (Jackson et al., 2016, 2019). Therefore, there is confidence that large scale changes
82 in North Atlantic Ocean circulation have occurred over the past few decades, and that they have had a significant
83 impact on upper ocean heat content.

84

85 Although there is consistency across proxies of AMOC changes in the North Atlantic, there are considerable gaps in
86 our understanding and major uncertainties to overcome. For example, the development of the subsurface density
87 proxies has been investigated so far in just a few models (Ortega et al., 2017; Robson et al., 2014). However, there is

88 considerable spread across climate models in the simulations of AMOC mean state and variability (Reintges et al.,
89 2017; Zhang and Wang, 2013), and also in the latitudinal coherence of AMOC anomalies (Li et al., 2019; Roberts et
90 al., 2020; Hirschi et al., 2020), which might reflect different roles of deep density anomalies in the western SPNA on
91 the AMOC, as well as different interplays between the subpolar and subtropical gyre contributions (Zou et al.,
92 2020). Models also do not resolve realistically many key features of AMOC, most notably the overflows, and this
93 affects the subsurface stratification downstream and on the western boundary (Zhang et al., 2011). There also
94 remains significant uncertainty for other important processes. For example, it is not yet clear whether the recent
95 changes in the SPNA are an ocean response to buoyancy forcing, or whether mechanical wind forcing has shaped
96 the recent observed changes (Robson et al, 2016; Piecuch et al. 2017). Local surface fluxes are also likely to explain
97 a significant proportion of the recent cooling (Josey et al, 2018). Subsurface density anomalies are not just a proxy
98 for the AMOC, but more generally for buoyancy forced (or thermohaline) circulation changes, including gyre
99 changes (Ortega et al., 2017; Yeager, 2015). Finally, the AMOC variability is also thought to respond to local wind
100 forcing on a range of timescales, especially at lower latitudes (Polo et al., 2014; Zhao and Johns, 2014), which could
101 disrupt or “mask” the influence of subsurface density anomalies as they propagate further south.

102

103 There is also considerable uncertainty in how and where subsurface density anomalies are formed in the SPNA, and
104 how they are related to the AMOC. In observations and models, most water transformation associated with the
105 AMOC occurs within the SPNA, and particularly in the eastern SPNA (Desbruyères et al., 2019; Grist et al., 2014;
106 Langehaug et al., 2012). However, subsurface density anomalies in the western SPNA on decadal timescales have
107 often been linked with buoyancy forcing and changes in deep convection in the Labrador Sea or with changes in the
108 volume of Labrador Sea Water production (Yashayaev and Loder, 2016; Yeager and Danabasoglu, 2014). Many
109 studies have also reported that the basin-wide AMOC in ocean-only and coupled models is sensitive to heat flux or
110 buoyancy forcing in the Labrador Sea (Kim et al., 2020; Ortega et al., 2011, 2017; Xu et al., 2019; Yeager and
111 Danabasoglu, 2014). Indeed, idealised experiments have shown that persisting positive NAO phases can strengthen
112 the AMOC by fostering deep water formation via increased surface cooling in the Labrador Sea, thus inducing
113 changes in the zonal density gradient (Delworth and Zeng, 2016; Kim et al., 2020), and thermal wind responses.
114 However, the real link between deep convection, deep water formation, and density anomalies at depth in the
115 Labrador Sea is complex, and not fully understood (Katsman et al., 2018). Observations suggest that very little
116 water transformation and deep water formation actually occurs in the Labrador Sea (Pickart and Spall 2007; Lozier
117 et al., 2019). Indeed, recently it has been shown that the Labrador Sea (i.e. OSNAP-west) played very little role in
118 the interannual variability so far observed across the whole OSNAP line (Lozier et al., 2019), with the Irminger Sea
119 playing a more dominant role. The Irminger Sea is a region that in some models controls the AMOC and SPNA
120 variability, and that is especially sensitive to advective processes (Ba et al., 2013) and Arctic overflows (Fröb et al.,
121 2016). Moreover, ocean-only models appear to significantly overestimate the amount of deep water formed within
122 the Labrador Sea, with likely implications for coupled models (Li et al., 2019). These inconsistencies raise the
123 question of whether models are simulating the right relationships.

124

125 In this study we will address some of the above uncertainties by performing a multi-model analysis of the North
126 Atlantic in coupled climate models. We focus on the question of how robust is the relationship between subsurface
127 Labrador Sea density anomalies and the basin-wide Atlantic Ocean circulation on decadal timescales. We also assess
128 the question of whether Labrador Sea density can robustly induce density changes over the western continental slope
129 and generate a geostrophic response in the meridional circulation (Bingham and Hughes, 2009; Roussenov et al.,
130 2008). Shedding new light on these links is important for, among other reasons, determining to what extent the
131 RAPID measurements represent the variability of the basin-wide AMOC cell, as well as to identify the models that
132 can produce more reliable predictions and projections of the SPNA. For this, we will assess specifically the
133 connection between subsurface density and AMOC at high and low latitudes via the western boundary. Furthermore,
134 we will determine whether models consistently support an impact of AMOC changes on the SPNA upper ocean
135 temperatures, and if not, investigate why. Our primary aim is to provide, for the first time in a multi-model context,

136 a broad characterization of these relationships using consistent analysis frameworks and tools, and to document the
137 uncertainty. The reasons for the uncertainty in the relationships will also be explored, establishing links with key
138 model climatological properties that could eventually be exploited as emergent constraints. We intentionally do not
139 explore in detail how subsurface density anomalies are formed in these models, and leave this for further study.

140

141 The paper is organised as follows. Section 2 describes the experiments and methods. Labrador Sea density, and its
142 link with the ocean circulation and the wider North Atlantic are explored across the multi-model ensemble in
143 Section 3. The characteristics of the intermodel spread in the previous relationships are explored in Section 4, and
144 Section 5 presents the main conclusions of this study and discusses its implications.

145

146

147 **2. Experiments and methods**

148

149 Here we provide an overview and brief description of the models used in this study and provide some statistical
150 considerations for the intermodel comparison.

151

152 **2.1. Experiment selection**

153

154 For the multi-model analysis, we use the preindustrial control simulations (picontrol) from the fifth phase of the
155 Coupled Model Intercomparison Project (CMIP5; Taylor et al. 2012), in which forcing values of GHGs, aerosols,
156 ozone and solar irradiance are fixed to 1850 levels. We chose to use control over historical simulations to focus
157 exclusively on internal variability and benefit from the more robust statistics that the long preindustrial experiments
158 provide. Furthermore, we avoid the forced trends present in the historical experiments, which can lead to
159 correlations that are difficult to interpret objectively (Tandon and Kushner, 2015). From the CMIP5 ensemble, we
160 only use those models in which 3D fields of ocean temperature and salinity, as well as the streamfunctions of
161 meridional overturning circulation and/or the barotropic circulation, were available. Twenty different models meet
162 this condition. Their main characteristics and number of simulation years have been summarized in Table 1. Most of
163 the models have a nominal horizontal resolution in the ocean close to 1° , and, therefore, cannot resolve the effects of
164 eddies. Menary et al. (2015) has shown for these same model simulations that the effective horizontal resolution can
165 be higher over the Labrador Sea, due to the non-regular grids. Effective resolutions over the Labrador Sea area range
166 from 0.21° in the GC2 model to 1.1° in GISS-E2-R/GISS-E2-R-CC/CanESM2, with these differences determining
167 to a large extent the mean state model biases and the dominant drivers (i.e. salinity or temperature) of the Labrador
168 Sea density changes.

169

170 Complementing these simulations, we also consider two control experiments with eddy-permitting resolutions.
171 Specifically, we use a present day control simulation (i.e. with fixed radiative forcing levels from year 1990) of the
172 HiGEM model, with nominal horizontal resolution in the ocean of $1/3^\circ$, and of 0.83° latitude \times 1.25° longitude in
173 the atmosphere (Shaffrey et al., 2009), and a pre-industrial control of HadGEM3-GC2 (hereafter, GC2; Ortega et al.
174 2017) with a nominal resolution in the ocean of $1/4^\circ$ (ORCA025) and N216 in the atmosphere (i.e. approximately 60
175 km in the mid-latitudes). The GC2 simulation is the same one employed for the previous analyses of Labrador Sea
176 variability in Robson et al. (2016) and Ortega et al. (2017). Note that we will assume that the present day control in
177 HiGEM can be compared with the other preindustrial simulations due to the large uncertainty these later show in
178 their climatological biases, and so, for the sake of simplicity, we will only refer to preindustrial control experiments
179 from now on. [Figure 1](#) demonstrates that this assumption is reasonable, since the mean Labrador Sea stratification in
180 HiGEM is very similar to that in the other models.

181

182 As an observationally-constrained reference, this study also includes the assimilation run from DePreSys3, a decadal
183 prediction system from the MetOffice based on GC2 (Dunstone et al., 2016). In the ocean, the assimilation is

184 performed through a strong nudging (ten-day relaxation timescale) towards the full fields of a three-dimensional
 185 objective temperature and salinity analysis (Smith and Murphy, 2007). Since it covers a comparatively shorter
 186 period (1960-2013), and therefore different timescales than the control experiments, its comparison with the other
 187 simulations will be done with caution, in particular regarding the indices of the large-scale Atlantic circulation, for
 188 which other assimilation products show important discrepancies (Karspeck et al., 2015), thus highlighting
 189 significant uncertainty. For evaluation purposes, we also use EN4.2.1 (Good et al., 2013), an objective analysis of
 190 monthly temperature and salinity 3D observations developed at the MetOffice.

191
 192
 193
 194

Table 1: List of the models used for this study, their characteristics and those of their picontrol simulations. For further details on the CMIP5 model configurations and components please refer to Table 9.A.1 in Flato et al. (2013) and references therein.

Model ID	Lon x Lat ocean resolution (number of vertical levels)	Length	Key variables available
HadGEM3-GC2	1/4° x 1/4° (75 levels)	311 years	AMOC, SPGSI, LSD, NOHT
HiGEM	1/3° x 1/3° (40 levels)	341 years	AMOC, SPGSI, LSD, NOHT
ACCESS1-0	1° x 1° enhanced near Equator and high latitudes (50 levels)	500 years	SPGSI, LSD, NOHT
ACCESS1-3	1° x 1° enhanced near Equator and high latitudes (50 levels)	500 years	SPGSI, LSD, NOHT
CCSM4	1.125° x 0.27–0.64° (60 levels)	1051 years	AMOC, SPGSI, LSD
CESM1-BGC	1.125° x 0.27–0.64° (60 levels)	500 years	AMOC, LSD
CESM1-CAM5	1.125° x 0.27–0.64° (60 levels)	319 years	AMOC, LSD
CESM1-FASTCHEM	1.125° x 0.27–0.64° (60 levels)	222 years	AMOC, LSD
CESM1-WACCM	1.125° x 0.27–0.64° (60 levels)	200 years	AMOC, LSD
CNRM-CM5	0.7° x 0.7° (42 levels)	850 years	AMOC, SPGSI, LSD
CanESM2	1.4° x 0.93° (40 levels)	996 years	AMOC, SPGSI, LSD
FGOALS-g2	1° x 1° with 0.5° meridional in the tropical region (30 levels)	700 years	AMOC, LSD
FGOALS-s2	1° x 1° with 0.5° meridional in the tropical region (30 levels)	501 years	SPGSI, LSD, NOHT
GFDL-ESM2G	1° x 0.85° (63 levels)	500 years	SPGSI, LSD
GISS-E2-R	1.25° x 1° (32 levels)	550 years	AMOC, LSD
GISS-E2-R-CC	1.25° x 1° (32 levels)	251 years	AMOC, LSD
MPI-ESM-LR	1.5° x 1.5° (40 levels)	1000 years	AMOC, SPGSI, LSD

MPI-ESM-MR	0.4° x 0.4° (40 levels)	1000 years	AMOC, SPGSI, LSD
MPI-ESM-P	1.5° x 1.5° (40 levels)	1156 years	AMOC, SPGSI, LSD
MRI-CGCM3	1° x 0.5° (51 levels)	500 years	AMOC, LSD, NOHT
NorESM1-M	1.125° x 1.125° (53 levels)	501 years	AMOC, SPGSI, LSD, NOHT
NorESM1-ME	1.125° x 1.125° (53 levels)	252 years	AMOC, SPGSI, LSD, NOHT

195

196

2.2. Methodological considerations

197 Density values are computed from 3D salinity and potential temperature fields, using the International Equation of
 198 State of seawater (EOS-80), and are referred to the level of 2000 dbar (σ_2), to give a stronger emphasis to the deep
 199 water properties.

200 Statistical significance of correlation coefficients is assessed following a two-tailed Student's t-test that takes into
 201 account the series' autocorrelation to correct the sample size, reducing the degrees of freedom of a series to its
 202 effective value (Bretherton et al., 1999).

203 Because our goal is to provide further insight into the suggested relationships established from observed trends in
 204 the North Atlantic (e.g., Robson et al., 2016), all statistical analyses in this study exploring the relationships between
 205 variables and associated lags are based on 10-year running trends. This is analogous to the calculation of a typical
 206 10-year running mean, but computing over each 10 year period a linear trend instead and keeping the slope value.
 207 Note also that our main results remain similar if decadal running means are applied instead (not shown), as both are
 208 alternative approaches to concentrate on the low-frequency variability. Running trends have also the particular
 209 advantage of not being sensitive to long-term drifts, which are still present (and can be important for some
 210 simulations and variables) when running means are computed. To illustrate how decadal running trends represent
 211 low-frequency variability, and how they compare with the decadal running means, both have been included in
 212 [Figure 2b](#) (solid thick lines vs dashed thin lines) for an index of Labrador Sea density.

213

214 3. Labrador Sea density as an index of multi-decadal North Atlantic variability

215

216 This section explores the potential of Labrador Sea density as a proxy of the ocean circulation changes in the North
 217 Atlantic. As in our previous studies (Ortega et al., 2017; Robson et al., 2016), the indices that we will herein define
 218 represent waters within the Labrador Sea and not those that are necessarily formed in the region (e.g. Labrador Sea
 219 Water). Since Labrador Sea variability is affected by different processes (e.g. vertical mixing, Arctic-Atlantic
 220 overflows, sea ice interactions) that can be represented differently in the models, both in time and space, we
 221 characterize its variability over a relatively broad box (60°W-35°W; 50°N-65°N, blue box [Figure 1a](#)) that also
 222 includes part of the Irminger Sea region. Note that over this large area EN4.2.1, shows the weakest density
 223 stratification in the North Atlantic (characterised in [Figure 1a](#) as the density difference between 1000m and the
 224 surface).

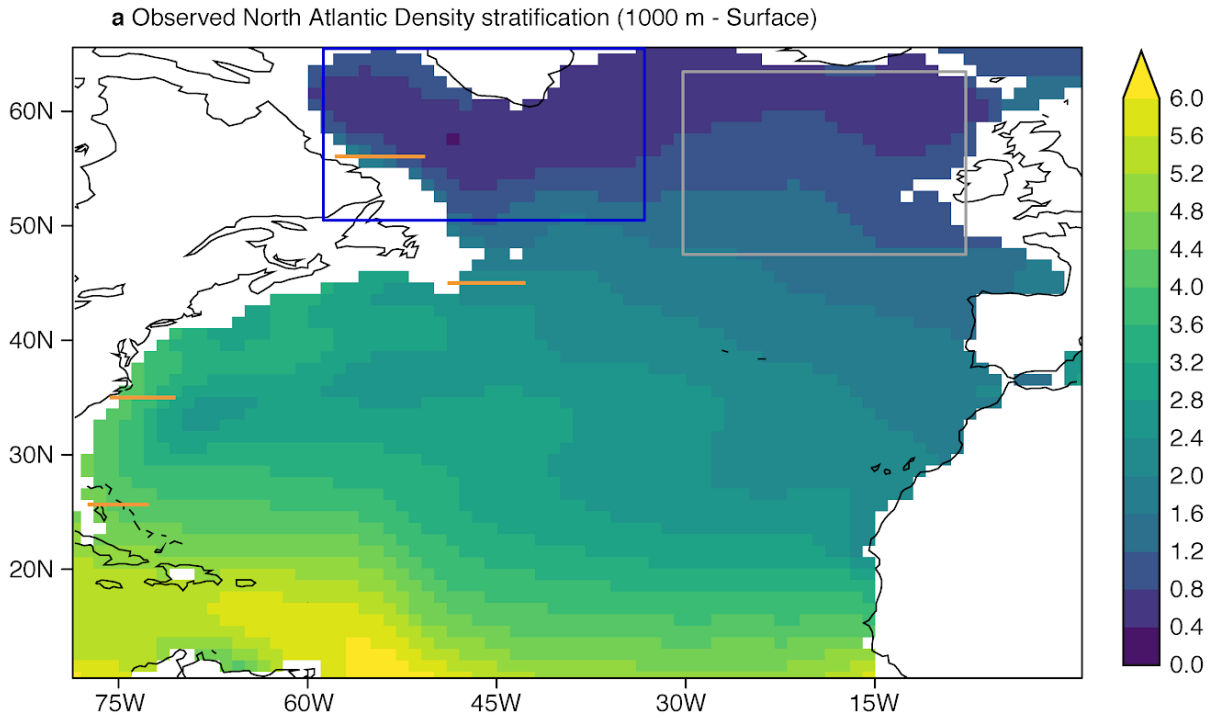
225 3.1. Labrador Sea density across models

226 A first indicator of potential model discrepancies is Labrador Sea stratification, which can lead to differences in the
 227 representation of deep ocean convection (i.e. weaker density stratifications will facilitate the mixing, fostering
 228 convection activity, and vice versa for stronger density stratifications). [Figure 1b-d](#) illustrates the inter-model

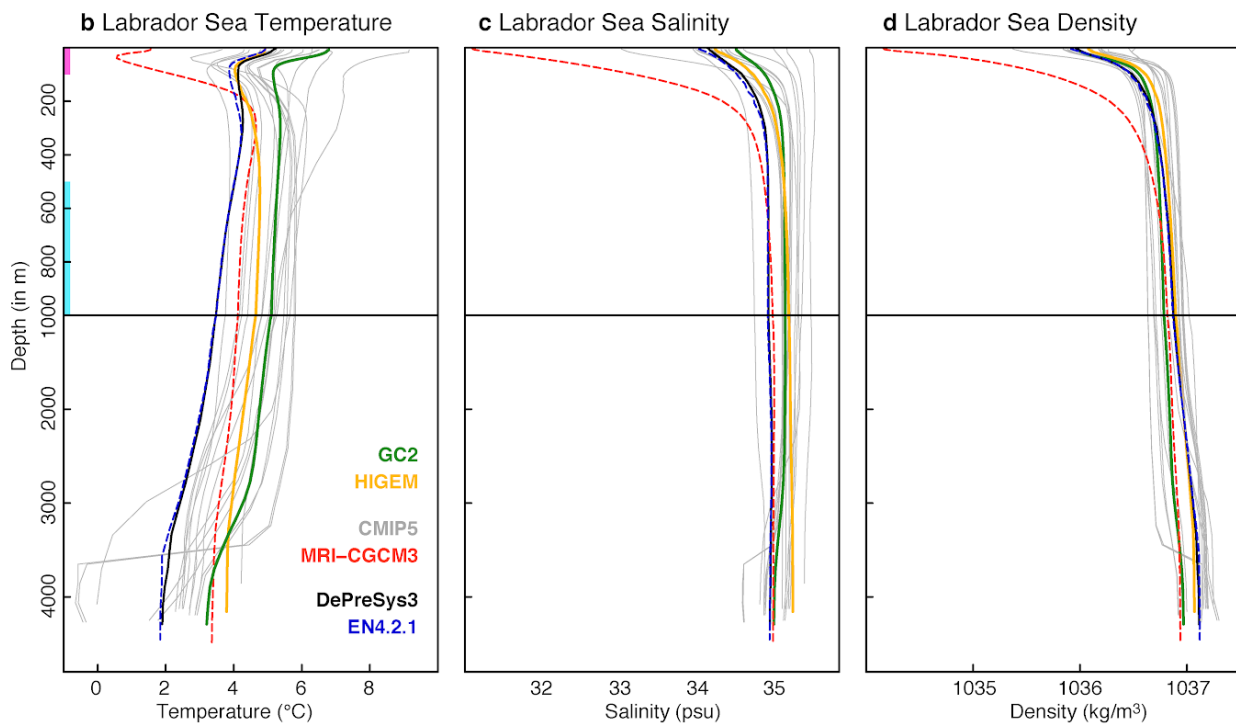
229 differences with the vertical profile of the spatially averaged Labrador Sea temperature, salinity and density. The
230 largest discrepancies are seen for temperature. Most models present their warmest waters at the surface, and
231 temperatures decrease sharply to minimum values around 100 m and increase again at deeper levels, reaching
232 uniform conditions after approx 300 m. However, the location and magnitude of this temperature minimum and the
233 two maxima are highly variable. It is important to note that the profile for one of the models, MRI-CGCM3, is
234 noticeably different to the others, with a subsurface minimum more than 2 degrees colder than for any of the other
235 models. In terms of salinity, the general profile is more coherent across models, with minimum salinity at the surface
236 that progressively increases with depth and attains uniform values after 500 m. Density stratification seems to be
237 determined by salinity, as their two vertical profiles show similar features. This similarity includes exceptionally
238 strong density and salinity stratification in MRI-CGCM3 as compared with the other models. This stratification is so
239 strong that it precludes the occurrence of deep convection (not shown). Because of this, MRI-CGCM3 is an outlier
240 for many of the metrics used in the paper, and has been excluded for the subsequent analyses to facilitate the
241 interpretation of our results. We also note that the profiles for the two eddy-permitting models (green and orange
242 lines in [Figure 1b,d](#)) lie within the spread of the CMIP5 models, indicating that resolution (at least to
243 eddy-permitting spatial scales) does not drastically change stratification in the region. The DePreSys3 assimilation
244 run closely matches the stratification in EN4.2.1, which supports DePreSys3 assimilation run as a reasonable
245 observation-constrained reference for the models. The comparison of both observation-based datasets with the rest
246 of simulations suggests that, in the subsurface, all models are too warm and most of them are too salty, two biases
247 that have a competing effect on the mean subsurface density. Because of these canceling effects, several models
248 show a comparatively better representation of the subsurface densities when compared to EN4.2.1 and DePreSys3.
249 This compensation of model shortcomings for temperature and salinity is clearly illustrated in HiGEM, which shows
250 a remarkable agreement with EN4.2.1 below 500 m.

251 To represent the characteristic interannual variability of Labrador Sea densities (hereafter referred to as LSD for
252 consistency with previous work), we perform an Empirical Orthogonal Function (EOF; Storch and Zwiers, 1999)
253 analysis and extract the leading mode for the spatially averaged annual means of LSD ([Figure 2a](#)), as in Ortega et al.
254 (2017). For all simulations the first EOF of LSD exhibits a vertical structure where density values are largest at or
255 near the surface and gradually decrease with depth. Thus, this first EOF typically reflects situations in which the
256 density stratification, as described by the climatological vertical profile in [Figure 1c](#), is weakened or strengthened,
257 which happens when the corresponding principal component takes positive and negative values, respectively. Some
258 inter-model discrepancies are evident, in particular regarding the depths where the maximum density values are
259 found, which can happen between the surface and 500 m. Despite these differences, the dominant timescales of LSD
260 variability seem to coincide between models. For example, [Figure 2b](#) illustrates the first principal component of
261 LSD (PC1-LSD) for GC2 and HiGEM, showing in both cases clear multidecadal variability. Furthermore, [Figure 2c](#)
262 shows the Fourier spectrum analysis of the annual PC1-LSD values, and most models show enhanced PC1-LSD
263 variability for periodicities between 5 and 30 years.

264 In addition to the PC1-LSD index we consider a deep LSD index as introduced in Robson et al (2016). The deep
265 LSD index is defined as the 1000-2500 m vertical mean of the spatially averaged density over the same region as
266 PC1-LSD. We now compare how both indices represent the low-frequency changes in LSD, described in this paper
267 as decadal running trends. A lead-lag correlation between the decadal trends in both PC1-LSD and deep LSD
268 indices shows that they are strongly correlated in all models. However, some differences emerge when considering
269 the lag of maximum correlation ([Figure 2d](#)). This comparison might indicate, once again, that decadal variability of
270 subsurface density is concentrated at different depths in different models. It is also possible that both indices are
271 sensitive to changes in deep water formation in different locations (e.g. Irminger or GIN Seas), which could, hence,
272 affect the depth and maximum lag of the correlations. Nevertheless, we adopt PC1-LSD for the rest of the analyses,
273 as it has the advantage of adjusting in each model to the depths in which density variability is more prominent.

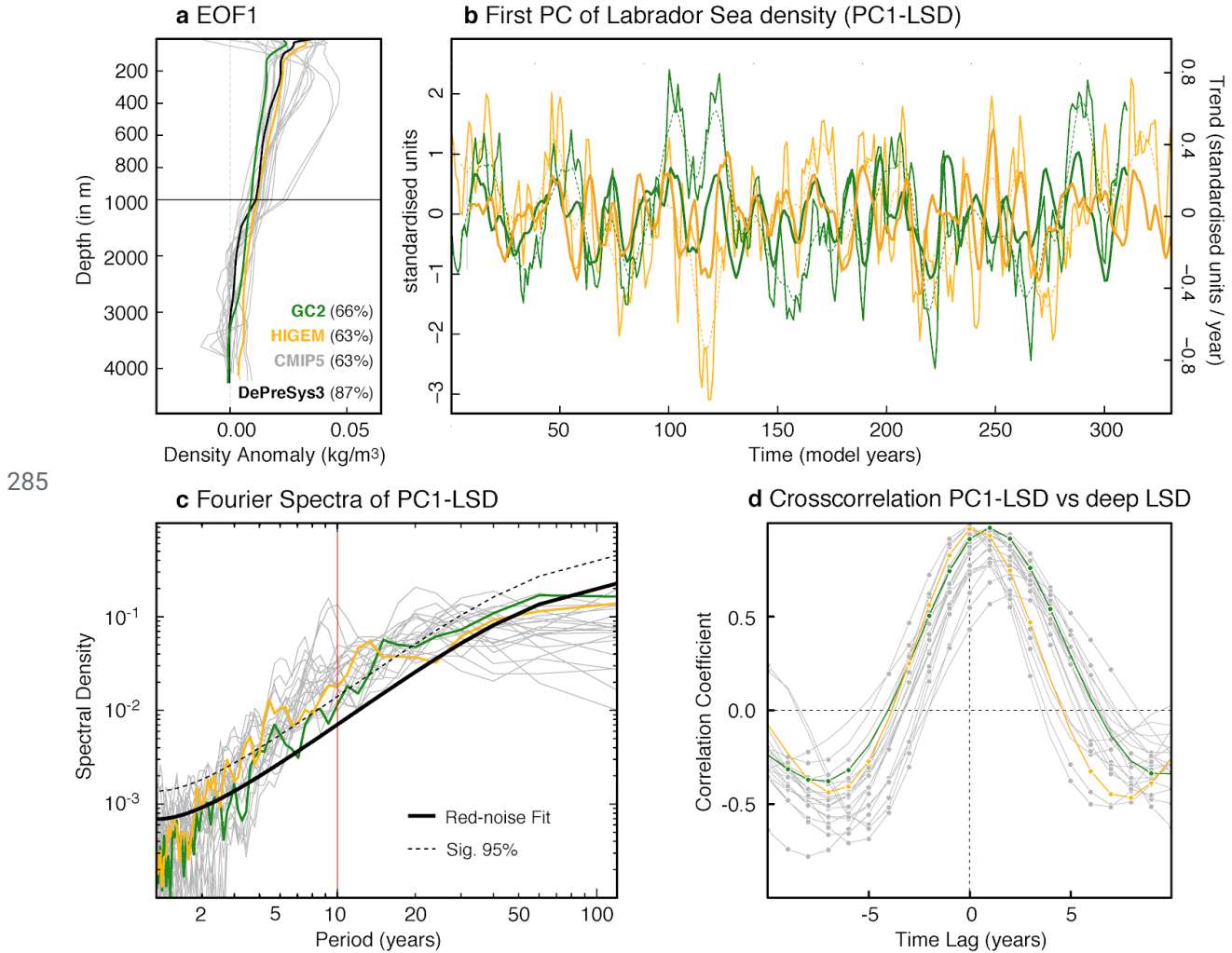


274



275 **Figure 1:** **a** Climatological density (computed as σ_2 at all depth levels) difference between the subsurface (1000m)
 276 and surface in the North Atlantic in the observational dataset EN4.2.1 (Good et al., 2013). The reference period to
 277 compute the climatology is 1960-2013. The grey box (32°W - 10°W and 47°N - 63°N) encloses the region where the
 278 ESPNA-T700 index in [Figure 4d](#) is computed. **b-d** Climatological mean of the spatially averaged Labrador Sea
 279 (60 - 35°W , 50 - 65°N , blue box in panel *a*) temperature, salinity and density as a function of depth in the simulation
 280 ensemble, the DePreSys3 assimilation run and EN4.2.1. The magenta (cyan) bars in the vertical axis correspond to

281 the depths that have been used to define the vertical stratification Labrador Sea indices. The horizontal orange lines
 282 by the North American coast represent the location of the latitudinal cross-sections in [Figure 10](#) and [Figure 11](#). For
 283 each model and dataset the climatology is computed for its whole length exceptv for EN4.2.1, that is computed for
 284 the overlap period with the DePreSys3 assimilation run.



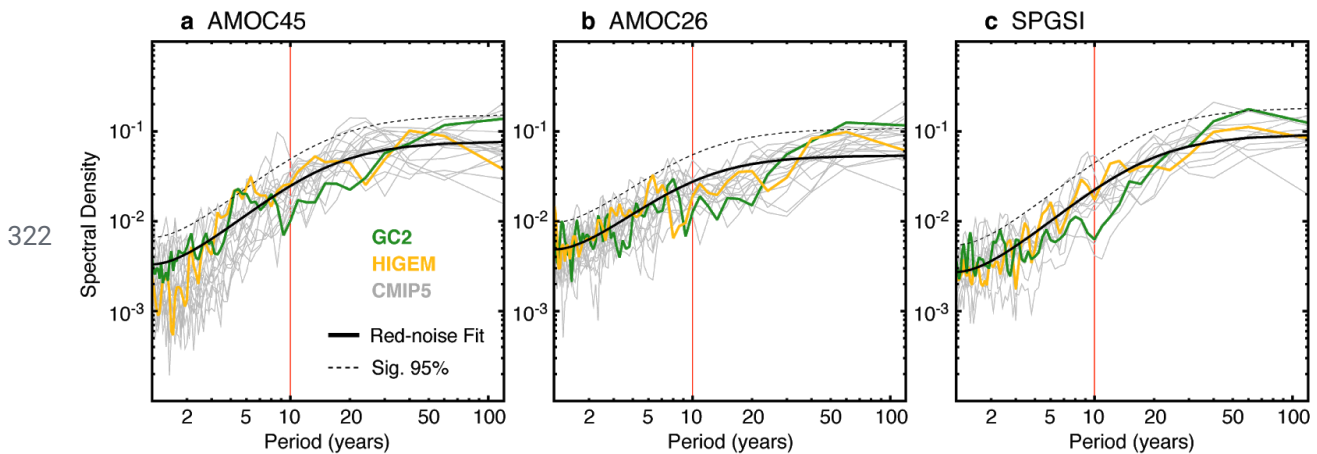
285

286 **Figure 2:** **a** First empirical orthogonal function (EOF) as a function of depth of the spatially averaged LSD in all the
 287 preindustrial experiments and in the DePreSys3 assimilation run. The percentage of variance explained by this mode
 288 in each model is included in brackets in the legend (for the CMIP5 runs, this represents the mean value across the
 289 ensemble). **b** Associated principal component of the spatially averaged LSD (PC1-LSD) in the two high-resolution
 290 experiments. The thin solid lines represent the raw yearly-resolved PC1-LSD timeseries, the thin dashed lines their
 291 respective 10 year running means, and the thick (and slightly darker) lines their associated 10-year running trends
 292 (centered around the last year of the decade over which the trend is computed). **c** Normalized Fourier spectra of the
 293 PC1-LSD index in each of the preindustrial simulations. The black thick line represents a red noise process with the
 294 same first autoregressive (AR1) coefficient as PC1-LSD in GC2, and the dashed line sets the 95% confidence
 295 interval of this red-noise process. No major differences are found when using HiGEM’s AR1 coefficient instead.
 296 The red vertical line highlights the 10 year periodicity to separate the interannual from the decadal to multi-decadal
 297 timescales. **d** Lead-lag correlations between the decadal trends in PC1-LSD, and those in the deep LSD index from
 298 Robson et al. (2016), defined as the 1,000–2,500 m average density in the box 60–35°W, 50–65°N. Positive lags

302 indicate that PC1-LSD leads the changes in deep LSD. Full dots denote correlation values exceeding a 95%
 303 confidence level based on a student's t-test that takes into account the series autocorrelation.

301 3.2. Labrador Sea density linkages with the ocean circulation

302 The link between PC1-LSD and other ocean circulation indices in the North Atlantic is now examined. Three
 303 indices are considered: the AMOC at two different latitudes, 26°N (i.e. the same latitude as the RAPID array) and
 304 45°N to capture the typical variability of the subpolar AMOC, and an index of the subpolar gyre strength. The
 305 AMOC indices are computed as the maximum of the North Atlantic overturning circulation at any depth.
 306 Furthermore, the Ekman component is removed to focus on the slow wind-forced and the thermohaline-driven (i.e.
 307 the only one that can be influenced by the PC1-LSD directly) AMOC changes. To compute the Ekman component,
 308 we vertically integrate the Ekman velocities (after introducing a depth-uniform return flow to ensure no net
 309 meridional mass transport), following Eq. 6 in Baehr et al. (2004) with a fixed Ekman layer depth of 50 meters. This
 310 Ekman component is then removed at each depth level, prior to the calculation of the AMOC indices. The subpolar
 311 gyre strength is computed as an average of the North Atlantic barotropic streamfunction in the Labrador Sea region
 312 (60–35°W, 50–65°N), where the gyre strength is usually maximum. Since the SPG circulation is cyclonic and,
 313 therefore, associated with negative barotropic streamfunction values, the subpolar gyre strength index (SPGSI) is
 314 multiplied by -1 so that an intensification of the gyre corresponds to a positive value of the index. The Fourier
 315 spectra of the raw ocean circulation indices (Figure 3) show that, similar to the PC1-LSD, all three indices have
 316 strong multidecadal variability, with the largest differences with respect to PC1-LSD emerging for the timescales
 317 between 10 and 30 years, in which the spectral power is comparatively weaker, in particular for the AMOC26 index,
 318 and at 50 and longer timescales, in which the ocean circulation indices appear to have enhanced variability with
 319 respect to PC1-LSD. Similar spectra, but with enhanced variance at short timescales and reduced variance at the
 320 longest timescales are obtained for the AMOC indices when the Ekman component is kept (Supplementary Figure
 321 1), which suggests that the low-frequency processes dominate the total AMOC variability.



323 **Figure 3:** a-c Fourier spectra in the picontrol ensemble for the indices AMOC45, AMOC26 and SPGSI. Red-noise
 324 spectra corresponding to a 1st order autoregressive process fit to GC2 indices are provided as reference.

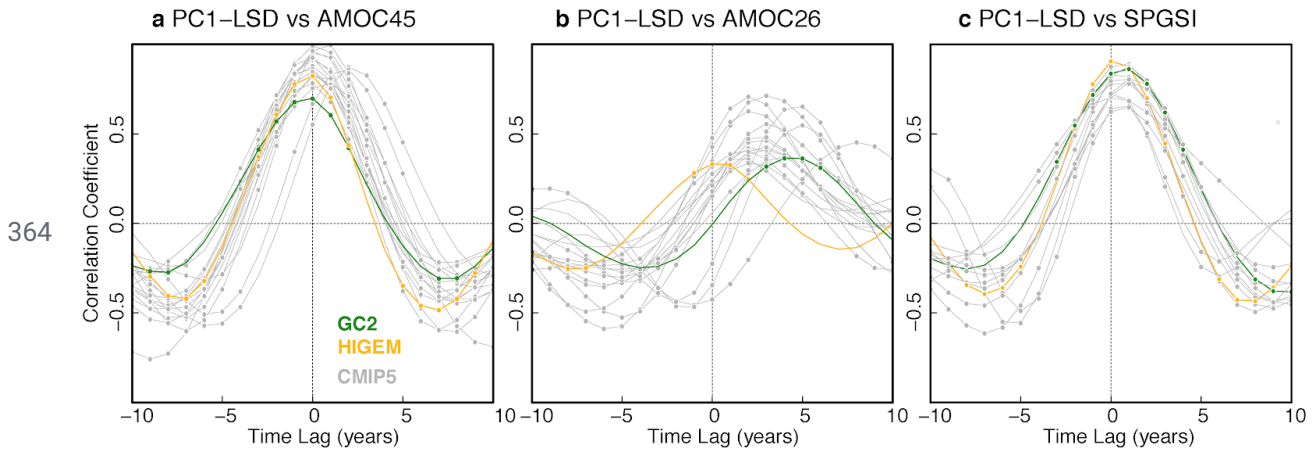
325 Figure 4a shows that decadal trends in PC1-LSD are associated with trends in the AMOC at 45°N (AMOC45).
 326 Nevertheless, there is some inter-model spread regarding the lag of maximum correlation, which ranges between 0
 327 and 2 years (with PC1-LSD leading), although both variables are in phase for the majority of models. The AMOC at
 328 26°N (AMOC26) is also positively related to PC1-LSD, with PC1-LSD leading AMOC26 by three years on average
 329 (Figure 4b). However, the average correlation between PC1-LSD and AMOC26 is weaker, and the spread in the
 330 magnitude and lag of the maximum correlation is larger than for AMOC45. Therefore, it appears that the link with

331 the subtropics is weaker than for 45°N and that AMOC coherence between subpolar latitudes and the subtropics in
332 coupled models is model dependent. This weaker link of PC1-LSD with the subtropical AMOC is not surprising, as
333 the LSD anomalies need to propagate a longer distance along the western boundary, allowing for model differences
334 in the representation of ocean currents and gyres to impact the timing and magnitude of the maximum correlations.
335 The reasons for the spread in the relationship between PC1-LSD and AMOC26 are explored in Section 4. A strong
336 relationship is also found between PC1-LSD trends and those in SPGSI ([Figure 4c](#)), of similar order than for
337 AMOC45. Thus, overall, PC1-LSD is a good proxy for the large-scale ocean circulation in the Subpolar North
338 Atlantic, and can also be a precursor for a fraction of the AMOC variability in the subtropical Atlantic.

339 PC1-LSD is also a good precursor of the full AMOC variability (i.e. including the Ekman transport), although the
340 wind-induced fluctuations associated with the Ekman component can introduce differences in the lags of the
341 maximum AMOC vs PC1-LSD correlations ([Supplementary Figure 2](#)). This different lag can be explained by the
342 fact that when the Ekman component is included, the AMOC contains a signal that is instantaneously driven by
343 basin-scale surface wind anomalies (such as the NAO) that are, ultimately, also linked to the heat loss in the
344 subpolar North Atlantic, which induces a delayed influence on the PC1-LSD (Ortega et al. 2017). Hence, including
345 Ekman can lead to counterintuitive relationships in some models in which the AMOC leads the PC1-LSD changes.
346 For that reason, and to ease the interpretation of the lagged-relationships, the rest of the analysis is exclusively
347 focused on the AMOC indices without ekman.

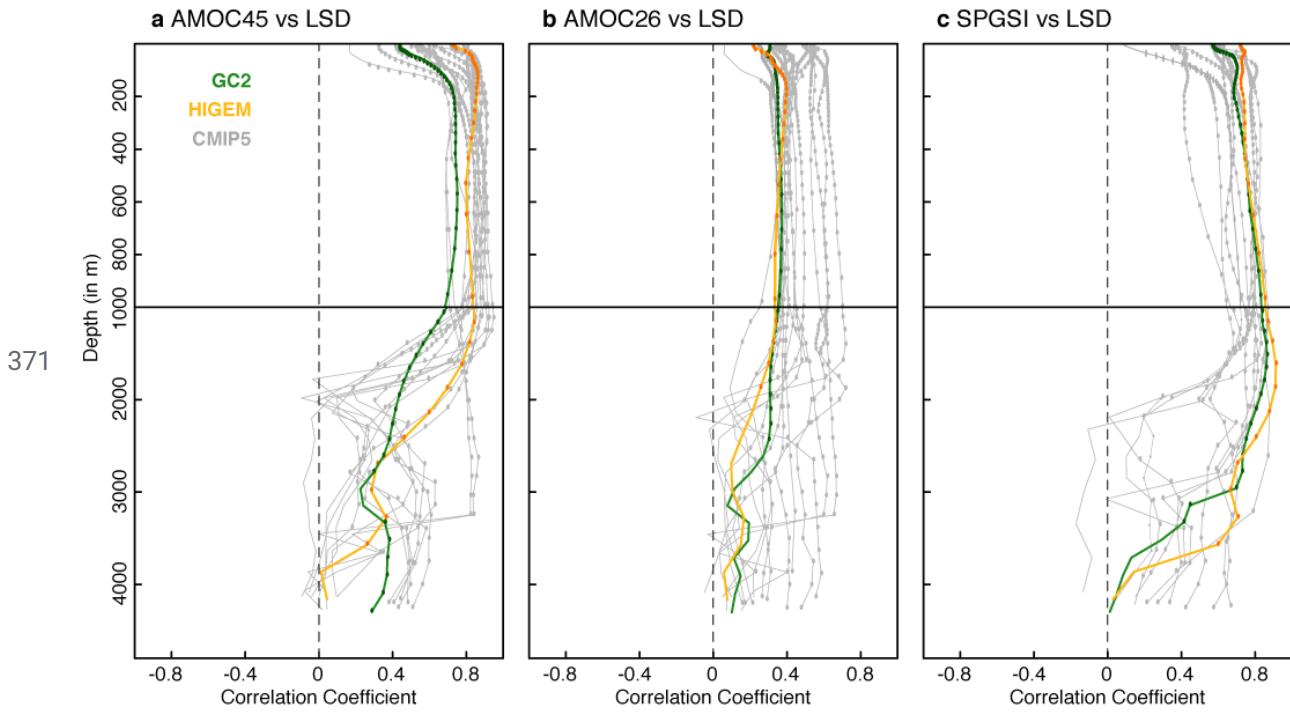
348 The role of PC1-LSD as a precursor of the AMOC is further supported by a parallel analysis in [Figure 5](#), looking at
349 the maximum correlation between the decadal AMOC trends and those in Labrador Sea density as a function of
350 depth, when the latter leads the AMOC by up to 10 years. [Figure 5](#) reveals that the strongest link between the
351 Labrador Sea densities and the AMOC, both at 45 and 26°N, occurs in its first 1000 m, the same levels where the
352 first EOF of LSD show the maximum loadings ([Figure 2a](#)), which confirms the appropriateness of using PC1-LSD
353 to represent the ocean circulation. The same analysis also supports a strong link between SPGSI and LSD, although
354 in that case the largest correlations usually happen at deeper levels (between 1000 and 2000 m). Note also that the
355 main conclusions drawn from PC1-LSD are also valid for the deep LSD index: however, the inter-model differences
356 are larger in the cross-correlations with the AMOC indices ([Supplementary Figure 3](#)). This difference could reflect
357 that the deep LSD index is more sensitive to other influences, like the Arctic overflows (Ortega et al., 2017), which
358 can be very differently represented across models. Overall, the PC1-LSD index seems to be a better choice to
359 describe multi-decadal North Atlantic variability in multi-model comparisons, as it selects the key depths for each
360 model. However, PC1-LSD is mostly focused on near surface levels and, therefore, likely represents mostly
361 Labrador Sea forced variability. Other indices describing densities at deeper levels might be preferable to compare
362 Labrador Sea Waters of different origins across models, and to evaluate their realism against observations.

363



365 **Figure 4: a** Lead-lag correlations across the picontrol ensemble between the PC1-LSD index and the maximum
 366 AMOC streamfunction at 45°N after the Ekman transport is removed (AMOC45). Correlations are based on 10-year
 367 running trends. Significance is assessed as in [Figure 2d](#) and indicated with a circle. For positive lags, PC1-LSD
 368 leads. **b-c** The same as in *a* but between PC1-LSD and the maximum AMOC streamfunction at 26°N after the
 369 Ekman transport is removed (AMOC26) and the subpolar gyre strength index (SPGSI).

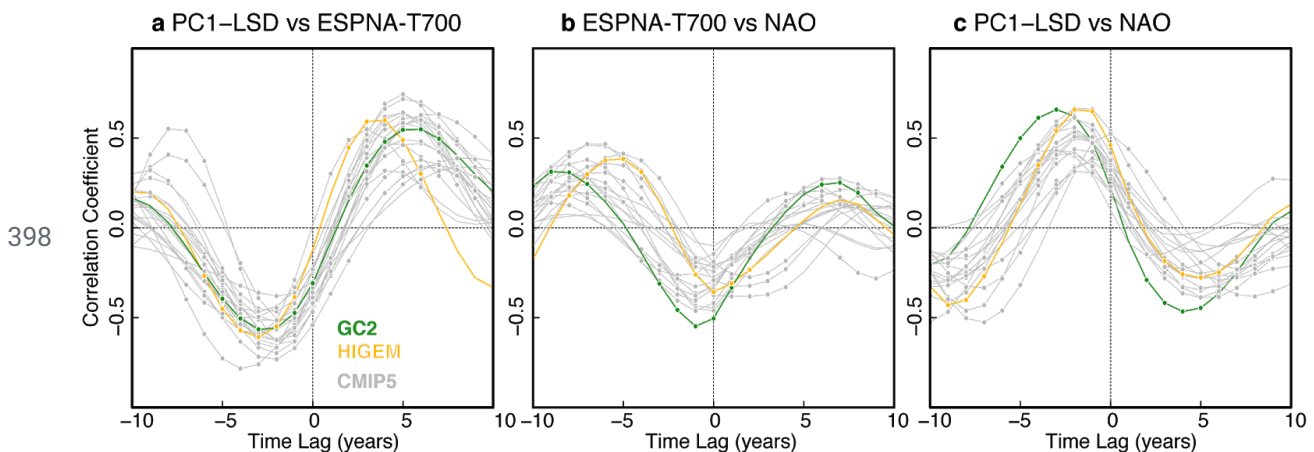
370



372 **Figure 5: a** Maximum correlation (for any lag between 0 and 10 years) between the AMOC45 index (after the
 373 Ekman transport is removed) and Labrador Sea Densities as a function of depth for all the simulations. Colored dots
 374 indicate correlations that are significant at the 95% confidence level. **b-c** The same as in *a* but between the
 375 AMOC26 index and LSD, and between the SPGSI and LSD, respectively.

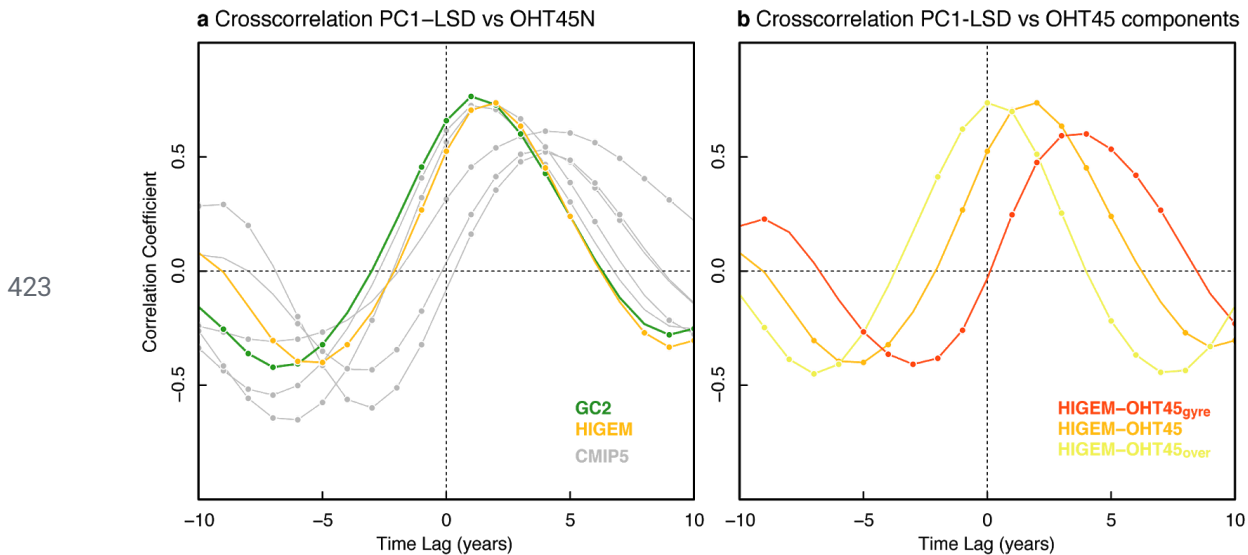
3.3. Labrador Sea density linkages with the wider North Atlantic

378 Previous studies based on the GC2 picontrol simulation have suggested LSD to be also a potential predictor of
 379 wide-spread cooling events in the eastern SPNA, like the observed cooling over 2005 to 2014 (Robson et al. 2016;
 380 Ortega et al. 2017). We thereby continue our exploration of the PC1-LSD index by investigating its link with the
 381 eastern SPNA in the multi-model ensemble. To explore this link we introduce a new index that represents the mean
 382 potential temperature in the eastern SPNA region (32°W - 10°W , 47°N - 63°N) averaged over the top 700 m of the
 383 ocean (ESPNA-T700). Lead-lag correlations between the decadal trends in PC1-LSD and this index (Figure 6a)
 384 show that there is a coherent relationship between both variables across models, with PC1-LSD increases
 385 (decreases) being consistently followed by ESPNA-T700 warmings (coolings). Nevertheless, there are inter-model
 386 differences concerning the magnitude and lag of the strongest positive correlations, revealing important uncertainty
 387 in the relationship. The spread in the PC1-LSD vs ESPNA-T700 relationship is thus reminiscent of the spread found
 388 between PC1-LSD and AMOC26, which suggests that they might be related. We also note significant negative
 389 correlations when ESPNA-T700 leads PC1-LSD by 2-4 years that might be explained by the opposed (and nearly
 390 concomitant) impacts that the NAO exerts on both variables (Figure 6b,c). Positive NAO phases, and associated
 391 surface buoyancy forcing (Lozier et al., 2008) lead in first instance to negative SSTs (Barrier et al., 2014; Lohmann
 392 et al., 2009) and an almost simultaneous cooling in ESPNA-T700 (Figure 6b). In comparison, on the western side
 393 of the SPNA, positive NAO phases contribute to reduce vertical density stratification, favoring convection and a
 394 more positive LSD index (Robson et al., 2016), which in the models lags the NAO by 2-3 years (Figure 6c). The
 395 fact that correlations between NAO and ESPNA-T700 are weaker than between PC1-LSD and ESPNA-T700
 396 suggests that the ocean might also be playing an additional role (besides the NAO) in controlling the ESPNA
 397 temperatures.



399 **Figure 6:** **a** Lead-lag correlations across the picontrol ensemble between the PC1-LSD index and the vertically
 400 averaged top 700 m temperatures in the eastern subpolar gyre (ESPNA-T700; grey box in Figure 1a). Correlations
 401 are based on 10-year running trends. Significance is assessed as in Figure 2d and indicated with a circle. For positive
 402 lags, PC1-LSD leads. **b-c** The same as in **a** but between the North Atlantic Oscillation (NAO; defined as the
 403 standardised difference in sea level pressure between the closest grid-points to Azores and Reykjavik) and the
 404 ESPNA-T700, and between the NAO and the PC1-LSD, respectively. In these two cases, for negative lags the NAO
 405 leads.

406 The link between PC1-LSD and the ESPNA could be explained through an influence of the PC1-LSD on the
 407 meridional ocean heat transport. This link is now investigated in the two eddy-permitting simulations (Figure 7) and
 408 in the five CMIP5 models for which the ocean heat transport fields are publicly available. In the two high resolution
 409 experiments and two of the CMIP5 ones the decadal trends in the meridional ocean heat transport at 45°N (OHT45)
 410 are strongly linked with those in PC1-LSD. This is a similar relationship to the one previously found in Figure 4
 411 between PC1-LSD and both the AMOC45 and SPGSI, but in this case with PC1-LSD leading with slightly longer
 412 lead time. The other CMIP5 experiments support a weaker, yet significant, link, as well as a longer lag between
 413 OHT45 and PC1-LSD. Altogether, Figure 7a confirms that PC1-LSD is a good precursor of the changes in the
 414 meridional ocean heat transport, although with some differences across models which might reflect a different
 415 representation of certain processes. The contributions of two different processes to this delay are further investigated
 416 in HiGEM, for which OHT had been decomposed online at each time-step into vertical and horizontal heat
 417 transports (as in Bryan, 1969), which can be respectively interpreted as the “overturning” (i.e. characterised by the
 418 zonal mean transport) and “gyre” (i.e. characterised by variations from the zonal mean transport) components
 419 (Robson et al., 2018a). While the overturning contribution ($OHT45_{over}$) increases in phase with the AMOC45,
 420 SPGSI and PC1-LSD changes (Figure 7b), the increase in the gyre component (OHC_{gyre}) starts four years later. That
 421 lag could be the time required in HiGEM for the propagation of mean and/or anomalous temperatures from the
 422 southern to the northern branch of the SPG.



424 **Figure 7:** **a** Lead-lag correlations in a subset of the picontrol experiments between the PC1-LSD index and the
 425 ocean heat transport across the 45°N transect (OHT45N). Note that the ocean heat content is only available for 5
 426 models of the CMIP5 ensemble. Correlations are based on 10-year running trends. **b** The same as in **a** but only in
 427 HiGEM for the different terms of the OHT45N. For positive lags, PC1-LSD leads.

428

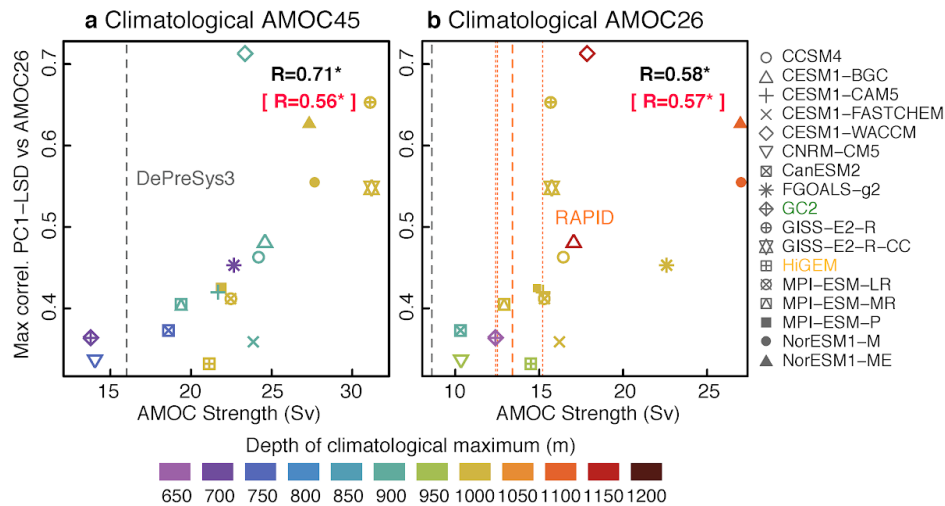
429 4. Characteristics of the inter-model spread in subpolar to subtropical AMOC

430

431 This section investigates which particular climatological model features are linked to the large inter-model spread in
 432 the PC1-LSD vs AMOC26 relationships. The most relevant model features thus identified will improve our process
 433 understanding, and can eventually be used to identify which models are most realistic and, in turn, can deliver more
 434 reliable projections of the future changes in the North Atlantic.

435 [Figure 8](#) shows that models that simulate a stronger and deeper climatological AMOC (both at 45°N and 26°N) tend
 436 to have a stronger correlation between PC1-LSD and the subtropics. All these linear relationships between
 437 climatological AMOC strength and depth and the PC1-LSD vs AMOC26 connectivity are significant at the 95%
 438 confidence level. These climatological AMOC values (without Ekman) can be put in context with those from
 439 RAPID observations and DePreSys3. RAPID observational uncertainties have been considered by including the
 440 mean values over three different non-overlapping periods (i.e. 2004-2007, 2008-2012 and 2013-2016; dotted lines in
 441 [Figure 8](#)). The scatterplots show that the majority of models whose climatological AMOC26 lies within the
 442 RAPID/DePreSys3 climatological spread have a relatively weak link between PC1-LSD and AMOC26, although
 443 some models supporting a strong link are also included or remain close to the RAPID/DePreSys3 values. However,
 444 caution is recommended, e.g., before defining emerging constraints, because model and observations are not directly
 445 comparable for numerous reasons. For example, both RAPID and DePreSys3 cover shorter periods than the
 446 simulations and relate to different background forcing conditions (present day vs preindustrial) which might imply
 447 different mean states (Thornalley et al., 2018). Also, climatological values of the AMOC26 strength are notably
 448 weaker in DePreSys3 than in RAPID, a difference that is not explained by the different temporal periods covered by
 449 each dataset (not shown) and that implies that DePreSys3 might be underestimating too the real AMOC45 strength.
 450 This underestimation might be larger than shown in [Figure 8](#), as evidence suggests RAPID calculations from
 451 mooring arrays might be underestimating the AMOC strength by ~ 1.5 Sv (Sinha et al., 2018).

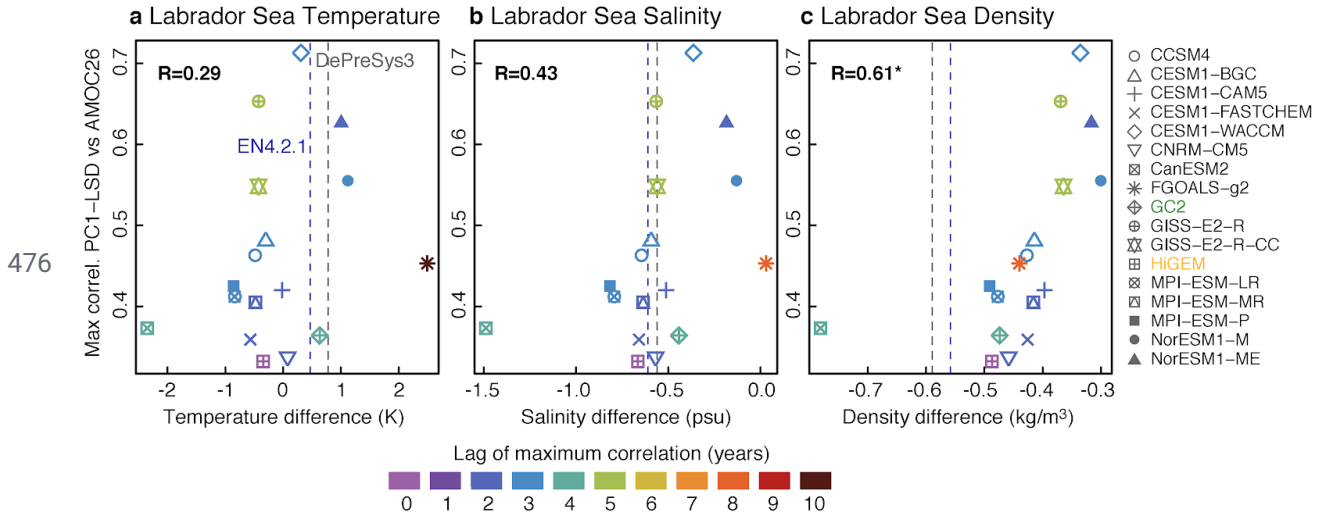
452



453 **Figure 8: a-b** Scatterplot of the maximum cross-correlation value in [Figure 4b](#) between PC1-LSD and AMOC26
 454 against the climatological AMOC45 and AMOC26 means, respectively. All AMOC indices refer to the values after
 455 the Ekman transport signal is removed. The maximum correlations are based on 10-year running trends, and always
 456 happen when PC1-LSD leads the AMOC26 index. Colors indicate the depth at which the climatological AMOC
 457 maximum occurs. The correlation coefficient between the maximum PC1-LSD correlation and the climatological
 458 mean AMOC is shown in the top-left corner in black. In magenta, the analogous correlation but against the depth of
 459 the mean climatological AMOC is shown. The presence of an asterisk indicates that the correlation is significant at
 460 the 95% confidence level. The dashed grey vertical lines mark the climatological AMOC strength value in the
 461 DePreSys3 assimilation run. The orange vertical lines indicate the climatological value from RAPID observations
 462 (Smeed et al., 2018) from 2004 to 2016 (dashed), and in three non-overlapping sub-periods of 4 years (dotted).

463 A potentially important factor behind the inter-model spread in [Figure 4b](#) is the mean density stratification in the
 464 Labrador Sea. [Figure 9](#) suggests that, indeed, the PC1-LSD vs AMOC26 spread is partly influenced by the density
 465 stratification in this region. Models that have a weaker density stratification (here defined as the difference between
 466 the top 100 m, and the average between 500-1000 m), and thus favor deeper convection in the Labrador Sea,

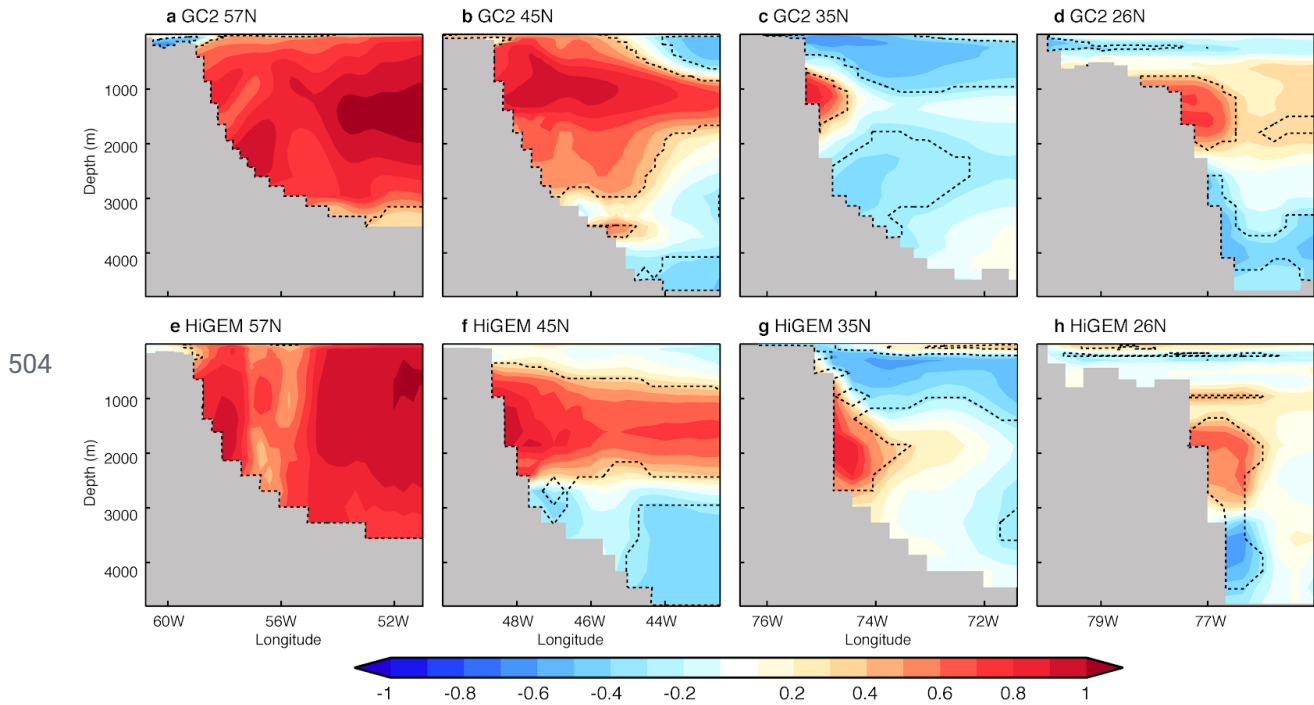
467 generally exhibit a stronger link between PC1-LSD and AMOC26. This result is robust for other stratification
 468 indices based on different depth levels (See [Supplementary Figure 4](#)). Differences in density stratification
 469 across-models can be due to a combination of different factors, from differences in the local buoyancy fluxes (driven
 470 by differences in the atmospheric circulation), to differences in the representation of the Arctic overflows, which are
 471 parameterised in some models (e.g. the CESM family; Danabasoglu et al., 2010), and explicitly resolved in others.
 472 No robust link between the PC1-LSD vs AMOC relationship and both temperature and salinity stratification in the
 473 Labrador Sea has been found. It is also worth mentioning that all models except CanESM2 are more weakly
 474 stratified in the Labrador Sea than the observations (represented herein by the DePreSys3 assimilation run and
 475 EN4.2.1). Hence, the real link of LSD with the AMOC26 may not be as strong as some models suggest.



477 **Figure 9:** **a** Scatterplot of the maximum cross-correlation value in [Figure 4b](#) between PC1-LSD and AMOC26
 478 (without the Ekman component) against the climatological mean of the Labrador Sea temperature stratification
 479 index (computed as the difference of the vertical means in the levels 0-100 m minus the vertical means in the levels
 480 500-1000 m; see Fig. 1). The maximum correlations are based on 10-year running trends. The correlation coefficient
 481 between the two metrics is shown in the top-left corner. The presence of an asterisk indicates that the correlation is
 482 significant at the 95% confidence level. Colors indicate the lag at which the maximum correlation between
 483 PC1-LSD and AMOC26 is obtained. The grey (blue) vertical lines depict the mean stratification value in the
 484 DePreSys3 assimilation run (EN4.2.1). In both cases, their overlap period is used to compute the climatology (i.e.,
 485 1960-2013). **b-c** The same as in **a** but for the Labrador Sea salinity and density (defined as σ_2), respectively.

486 Another key aspect of the PC1-LSD vs AMOC26 connectivity is the western boundary density (WBD). Indeed,
 487 boundary density is critical to the mechanism through which LSD influences the AMOC at lower latitudes. Positive
 488 (negative) LSD anomalies propagate equatorward following this boundary, and as they do so they strengthen
 489 (weaken) the zonal density gradient, triggering a thermal wind response that accelerates (decelerates) the AMOC. In
 490 the following we investigate differences in the propagation of boundary densities across models, and if these
 491 differences can affect the inter-model PC1-LSD vs AMOC26 spread. [Figure 10](#) focuses on the two high-resolution
 492 simulations, where important differences already manifest. It represents the in-phase correlations of PC1-LSD with
 493 the density fields (defined as σ_2) near the western boundary at four different longitudinal transects: 57°N (cutting
 494 across the Labrador Sea), 45°N, 35°N and 26°N. In both models, the depth of the maximum correlation near the
 495 continental shelf is coherent across latitudes. However, in HiGEM these occur at deeper levels (1000 to 3000 m)
 496 compared to GC2 (1000 to 2000 m), and the difference is especially clear at 35°N, where the highest correlations
 497 occur at ~2000 m in HiGEM, while only at 1000 m in GC2. Similar depth differences are also found at 26°N, but

498 with slightly weaker correlations. In addition to the difference in the depth of the maximum correlation between
 499 HiGEM and GC2, there are differences in the vertical structure between the two models. For example, at 35°N in
 500 GC2, density anomalies on the western boundary form a tripole (low correlation above and below the maximum
 501 correlation at ~1000 m), but in HiGEM the density anomalies form a dipole (Figure 10g). We note some differences
 502 in bathymetry at this latitude (which is steeper in HiGEM), which might partly explain some of the differences in
 503 terms of the density correlation structure.

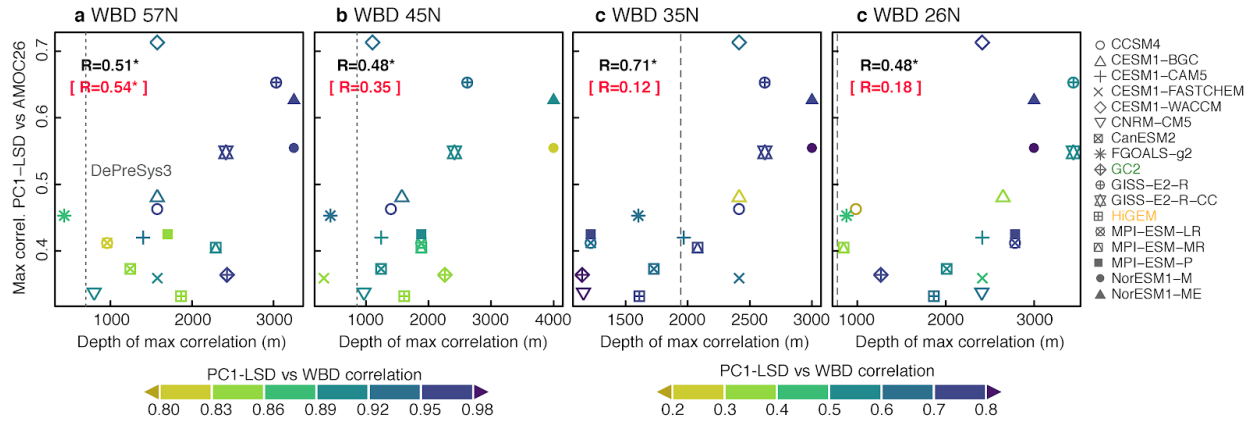


505 **Figure 10:** a In-phase correlation in GC2 between the PC1-LSD index and the density fields across a zonal section
 506 at 57°N located in the vicinity of the western Atlantic boundary. Thin dashed contours enclose areas where the
 507 correlation significance exceeds the 95% confidence level. Correlations are based on 10-year running trends. **b-d**
 508 The same as in *a* but for zonal sections at 45°N, 35°N and 26°N. **d-h** The same as in *a-d* but for HiGEM.

509

510 [Figure 11](#) shows that the diversity in the depth of these boundary densities is even more evident when including the
 511 CMIP5 models. The depth of the maximum correlation between PC1-LSD and the western boundary density at the
 512 four latitudinal sections relates linearly (and significantly at the 95% confidence level) across models with their
 513 PC1-LSD vs AMOC26 correlation. In this case, models exhibiting maximum correlations with the WBDs at deeper
 514 levels generally show stronger links between PC1-LSD and the subtropical AMOC. In DePreSys, our
 515 observationally-constrained reference (dashed grey lines in [Figure 11](#)), these maximum correlations tend to occur at
 516 relatively shallow levels when compared with the multi-model ensemble. We have also checked if models with
 517 stronger correlations with the WBDs (as represented by the PC1-LSD and WBD maximum correlations at every
 518 latitudinal section) also support a stronger link between the PC1-LSD and the AMOC, but this linearity assumption
 519 only holds true at 57°N (correlations in magenta in [Figure 11](#)). This suggests that the depth along which WBDs
 520 propagate southward, and/or the vertical structure of anomalies, are the key aspects to understand and potentially
 521 narrow down the spread.

522



523 **Figure 11:** a Scatterplot of the maximum cross-correlations value in [Figure 4b](#) between PC1-LSD and AMOC26
 524 (without the Ekman component) against the depth at which the maximum correlations at any lag between PC1-LSD
 525 and the WBD at 57°N occur. The maximum correlations are based on 10-year running trends. The correlation
 526 coefficient between the two metrics is shown in black the top-left corner. Likewise, another correlation coefficient in
 527 magenta is shown, computed between the PC1-LSD and AMOC26 maximum correlation and the PC1-LSD and
 528 WBD at 57°N maximum correlation. The presence of an asterisk indicates that the correlation is significant at the
 529 95% confidence level. Colors indicate the maximum correlation between PC1-LSD and the WBD. The grey vertical
 530 lines depict the corresponding depth of maximum correlation for the DePreSys3 assimilation run. **b-d** The same as
 531 in **a** but for the WBD at 45, 35 and 26°N, respectively.

532

533 5. Conclusions and discussion

534

535 This article has explored, in a multi-model context, the linkages between subsurface density in the subpolar North
 536 Atlantic (SPNA) and the ocean circulation further south. In particular, it has explored the role of Labrador Sea
 537 density (LSD) in driving Western Boundary Density anomalies (WBD) and the ocean circulation, and the impact on
 538 upper ocean temperature changes in the SPNA. The analysis was based on two control simulations with
 539 eddy-permitting models, a preindustrial one with HadGEM3-GC2 and a present day one with HiGEM, and on 20
 540 CMIP5 preindustrial experiments. Furthermore, where possible these characteristic model features have been
 541 computed in observational datasets, as well as in a simulation assimilating observations. The major findings are
 542 listed below:

543

- 544 - All the simulations show clear multidecadal variability in Labrador Sea density. There is also a close link
 545 between LSD and the strength of the subpolar Atlantic Ocean circulation, with positive density anomalies
 546 leading to a strengthening of the Atlantic Meridional Overturning Circulation (AMOC) at 45°N and the
 547 Subpolar Gyre (SPG) circulation.
- 548 - The relationship between anomalous LSD and the strength of the AMOC at 26°N - the latitude of the
 549 RAPID array measurements - is also positive in the simulations, but there are significant inter-model
 550 differences, both in the strength of the relationship and the lag of maximum correlation. This uncertainty
 551 implies that the connectivity of LSD with the subtropics and latitudinal AMOC coherence is
 552 model-dependent.
- 553 - The connectivity between anomalies in LSD and AMOC at 26°N is sensitive to different model features,
 554 including the strength and depth of the climatological AMOC maximum, the mean density stratification in
 555 the Labrador Sea, and the depths at which the LSD propagates southward along the western boundary.

556 Stronger LSD connectivity with the subtropics tends to occur in models with a stronger and deeper AMOC,
557 weaker Labrador Sea stratification and western boundary density propagating at deeper levels.

- 558 - Observationally derived constraints of the model based relationships tend to suggest that the link between
559 LSD and the subtropical AMOC is weak. This suggests that observations of AMOC via RAPID may not be
560 representative of the basin wide buoyancy forced AMOC variability. However, caution is advised because
561 simulations and observations are not directly comparable, and so significant uncertainty remains in
562 constraining the relationship between LSD and subtropical AMOC.
- 563 - The multi-model ensemble does also support a significant lagged relationship between LSD and the upper
564 ocean temperature in the eastern SPNA, in line with previous studies linking LSD to the recently observed
565 changes in the North Atlantic. However, models disagree regarding the strength of the link (correlations
566 between 0.3-0.7), and the maximum lag (3 to 10 years).

567

568 We have shown that, in coupled climate models at least, subsurface density anomalies in the western SPNA are an
569 important predictor of the wider North Atlantic ocean circulation and upper ocean temperature in the SPNA. This
570 importance on the ocean circulation is especially clear at the latitudes of the SPNA itself. Given the important role
571 of the wind in driving lower latitude AMOC anomalies, and the range of processes by which wind can act on the
572 AMOC (Duchez et al., 2014b, 2014a; Kanzow et al., 2010; Polo et al., 2014; Zhao and Johns, 2014) it is not
573 surprising that the relationship between LSD and AMOC at 26°N is much weaker. Nevertheless, the reasons behind
574 the large spread in these relationships across models is not so clear.

575 We have tried to constrain this uncertainty by looking at a range of observed metrics that may explain the spread in
576 the correlation strength, including the density anomalies on the western boundary, the stratification of the Labrador
577 Sea, and the mean-AMOC strength. Overall, these constraints point to a relatively weak relationship between LSD
578 and AMOC at 26°N on decadal timescales (i.e. $r \sim 0.4$) in the real world. However, there are many reasons why this
579 number is still very uncertain, and further work is needed to assess its validity. A caveat of this study is that the
580 simulations and observation-based datasets employed are not directly comparable, as they differ in the background
581 radiative forcing levels, the length of the period used to compute the climatologies, and even the way some indices,
582 like the AMOC, are computed. We also recognise that there is large uncertainty within the observationally derived
583 metrics. For instance, the assimilation run in DePreSys3, which is used to constrain relationships, clearly
584 underestimates the mean AMOC strength at 26°N with respect to RAPID (see [Figure 8b](#)) and, therefore, might be
585 also underestimating the AMOC at higher latitudes. Our findings might also be limited by model deficiencies. There
586 is emerging evidence that current models underestimate AMOC and North Atlantic variability on decadal timescales
587 (Roberts et al., 2013; Cheung et al., 2017;), which can degrade decadal predictability in the region and even lead to
588 overly weak linkages between the AMOC and the AMV (Yan et al., 2018). The AMV is indeed a mode of
589 variability that also shows important differences across models, in different aspects like its periodicity, amplitude,
590 spatial structure and climate footprints (Medhaug and Furevik, 2011; Zhang and Wang 2013; Kavvada et al., 2013),
591 inter-model differences that could be partly connected with those herein reported for the PC1-LSD vs AMOC
592 relationships. Models also tend to generally underestimate the depth of the return flow, and this may still affect how
593 density anomalies project on the basin-wide AMOC. It has also been argued that ocean-only models produce too
594 much deep water in the western basin and Labrador Sea (i.e., Li et al., 2019), and recent observations even challenge
595 the prevailing view from models that Labrador Sea convection dominates the AMOC variability (Koenigk and
596 Brodeau, 2017), suggesting that the key deep water formation occurs in the Irminger Sea, a few hundred kilometers
597 north east of the Labrador Sea (Lozier et al., 2019). Therefore, further in-depth study is warranted to narrow down
598 the uncertainty in the real AMOC and PC1-LSD relationship.

599 Most of the models considered in this study have relatively coarse resolution, including non-eddy oceans (\geq
600 $1^\circ \times 1^\circ$), which means that they might be missing some key dynamics for the AMOC (Johnson et al., 2019) that could
601 be important to represent realistic linkages. The current analysis also includes two models at eddy-permitting

602 resolution (HadGEM3-GC2 and HiGEM), whose relationships lie within the spread of those in the coarser models.
603 However, it could be that higher resolution is needed (e.g. enabling meso-scale eddies in subpolar latitudes) to
604 identify substantial differences (Hirschi et al., 2020; Johnson et al., 2019). A recent analysis based on
605 HadGEM3-GC3.1 (a later version of HadGEM3-GC2) configured at different horizontal resolutions has shown that
606 long-standing model biases affecting the North Atlantic are reduced at eddy-resolving resolution ($1/12^\circ \times 1/12^\circ$ in
607 the ocean), and that the strength of the AMOC, the boundary currents and the northward heat transport is higher than
608 for the coarser resolutions (Hirschi et al., 2020; Roberts et al., 2019). High resolution coupled models also generally
609 support the new view from OSNAP observations in which the largest fraction of AMOC variability (on sub annual
610 to decadal timescales) originates at the eastern SPNA (Hirschi et al., 2020). Eddy-resolving resolutions have also
611 been shown in a multi-model study (Roberts et al., 2020) to represent the AMOC response at 26°N differently in
612 future projections, leading to stronger declines than in non-eddying simulations, declines mostly associated with a
613 weakening in the Florida Current. Roberts et al. (2020) also compares the meridional coherence of the AMOC,
614 which does not seem to be resolution-dependent, a result that is in line with another multi-model comparison
615 between non-eddying and eddy-permitting simulations (Li et al., 2019).

616 Despite the current limitations in the models considered for this study, it is important to highlight that they provide a
617 rather consistent picture of a chain of relationships in the North Atlantic that is able to explain some of the recent
618 observed trends (Robson et al. 2016). This paper has broadly characterized this behaviour, and highlighted the
619 uncertainty. These relationships are also consistent with the mechanisms proposed by Yeager and Robson (2017) to
620 explain high levels of predictive skill in the SPNA on decadal timescales. Our analysis has also helped to identify
621 specific metrics (such as LSD stratification and the depth of the boundary density) that could be used as emergent
622 constraints for future projections, i.e. to subset the simulations expected to more realistically represent the future
623 changes in the region. Having a more realistic subpolar gyre stratification at present day conditions has been shown
624 in CMIP5 simulations to increase the probability of a future collapse in convection (Sgubin et al., 2017), that would
625 lead to a widespread SPG cooling. It remains to be tested if similar conclusions can be drawn from eddy-resolving
626 simulations.

627 **Code availability.** The main scripts used in the analysis and other supporting information that may be useful to
628 reproduce the results of this article are archived at the Barcelona Supercomputing Center and will be shared upon
629 request by the corresponding author.

630 **Data availability.** Outputs from the CMIP5 simulations can be downloaded from the corresponding ESGF node:
631 <https://esgf-node.llnl.gov/projects/cmip5/>. EN4 observations used in this study correspond to version 2.1 of the
632 dataset, available at <https://www.metoffice.gov.uk/hadobs/en4/download-en4-2-1.html>. Outputs from the GC2,
633 HiGEM and DePreSys3 simulations are available upon request to the corresponding author.

634 **Author contributions.** P. O., J. R. and R. S. conceived the study, which was later discussed and refined with the
635 other co-authors. M. M. downloaded and processed the CMIP5 data, computing the main climate indices. P. O. led
636 the analysis, and together with J. R. prepared the manuscript with contributions from all co-authors.

637 **Competing interests.** The authors declare that they have no conflict of interest.

638 **Acknowledgements.** We thank the UK Met Office for providing the model data of GC2 used in this study, and all
639 the research centers that contributed to CMIP5 and made their data available. This work was largely supported by
640 the NERC Projects “Dynamics and Predictability of the Atlantic Meridional Overturning and Climate Project”
641 (DYNAMOC, NE/M005127/1) and “Wider Impacts of Subpolar North Atlantic Decadal Variability on the Ocean
642 and Atmosphere” (WISHBONE, NE/T013516/1). P. O. work was additionally supported by the Spanish Ministry of
643 Economy, Industry and Competitiveness through the Ramon y Cajal grant RYC-2017-22772. J. R. was additionally

644 supported by the NERC ACSIS program and R. S. by NERC via the National Centre for Atmospheric Science
645 (NCAS).

646 **References**

647

648 Ba, J., Keenlyside, N.S., Park, W., Latif, M., Hawkins, E., Ding, H.: A mechanism for Atlantic
649 multidecadal variability in the Kiel Climate Model, *Clim. Dyn.*, 41, 2133–2144, 2013.

650

651 Baehr, J., Hirschi, J., Beismann, J.-O. and Marotzke, J.: Monitoring the meridional overturning circulation
652 in the North Atlantic: A model-based array design study, *J. Mar. Res.*, 62(3), 283–312,
653 doi:10.1357/0022240041446191, 2004.

654

655 Barrier, N., Cassou, C., Deshayes, J. and Treguier, A.-M.: Response of North Atlantic Ocean Circulation to
656 Atmospheric Weather Regimes, *J. Phys. Oceanogr.*, 44(1), 179–201, doi:10.1175/JPO-D-12-0217.1, 2014.

657

658 Bingham, R. J. and Hughes, C. W.: Geostrophic dynamics of meridional transport variability in the
659 subpolar North Atlantic, *J. Geophys. Res. Oceans*, 114(C12), doi:10.1029/2009JC005492, 2009.

660

661 Bretherton, C. S., Widmann, M., Dymnikov, V. P., Wallace, J. M. and Blad??, I.: The effective number of
662 spatial degrees of freedom of a time-varying field, *J. Clim.*, 12(7), 1990–2009,
663 doi:10.1175/1520-0442(1999)012<1990:TENOSD>2.0.CO;2, 1999.

664

665 Bryan, K.: Climate and the Ocean Circulation: III. The Ocean Model, *Mon. Weather Rev.*, 97(11),
666 806–827, doi:10.1175/1520-0493(1969)097<0806:CATOC>2.3.CO;2, 1969.

667

668 Caesar, L., Rahmstorf, S., Robinson, A., Feulner, G. and Saba, V.: Observed fingerprint of a weakening
669 Atlantic Ocean overturning circulation, *Nature*, 556(7700), 191–196, doi:10.1038/s41586-018-0006-5, 2018.

670

671 Cheung, A. H., Mann, M. E., Steinman, B. A., Frankcombe, L. M., England, M. H., & Miller, S. K.:
672 Comparison of Low-Frequency Internal Climate Variability in CMIP5 Models and Observations, *Journal of Climate*,
673 30(12), 4763–4776, 2017.

674

675 Danabasoglu, G.: On multidecadal variability of the Atlantic meridional overturning circulation in the
676 community climate system model version 3, *J. Clim.*, 21, 5524–5544, doi:10.1175/2008JCLI2019.1, 2008.

677

678 Delworth, T. L., & Zeng, F.: The Impact of the North Atlantic Oscillation on Climate through Its Influence
679 on the Atlantic Meridional Overturning Circulation, *Journal of Climate*, 29(3), 941–962, 2016.

680

681 Desbruyères, D. G., Mercier, H., Maze, G. and Danialt, N.: Surface predictor of overturning circulation
682 and heat content change in the subpolar North Atlantic, *Ocean Sci*, 15(3), 809–817, doi:10.5194/os-15-809-2019,
683 2019.

684

685 Dong, B. and Sutton, R. T.: Mechanism of interdecadal thermohaline circulation variability in a coupled
686 ocean-atmosphere GCM, *J. Clim.*, 18(1964), 1117–1135, doi:10.1175/JCLI3328.1, 2005.

687

688 Duchez, A., Hirschi, J. J.-M., Cunningham, S. A., Blaker, A. T., Bryden, H. L., de Cuevas, B., Atkinson, C.
689 P., McCarthy, G. D., Frajka-Williams, E., Rayner, D., Smeed, D. and Mizielinski, M. S.: A New Index for the
690 Atlantic Meridional Overturning Circulation at 26°N, *J. Clim.*, 27(17), 6439–6455, doi:10.1175/JCLI-D-13-00052.1,
691 2014a.

692

693 Duchez, A., Frajka-Williams, E., Castro, N., Hirschi, J. and Coward, A.: Seasonal to interannual variability
694 in density around the Canary Islands and their influence on the Atlantic meridional overturning circulation at 26°N,
695 *J. Geophys. Res. Oceans*, 119(3), 1843–1860, doi:10.1002/2013JC009416, 2014b.

696

697 Ducheze, A., Frajka-Williams, E., Josey, S. A., Evans, D. G., Grist, J. P., Marsh, R., McCarthy, G. D., Sinha,
698 B., Berry, D. I. and Hirschi, J. J.-M.: Drivers of exceptionally cold North Atlantic Ocean temperatures and their link
699 to the 2015 European heat wave, *Environ. Res. Lett.*, 11(7), 074004, doi:10.1088/1748-9326/11/7/074004, 2016.

700

701 Dunstone, N., Smith, D., Scaife, A., Hermanson, L., Eade, R., Robinson, N., Andrews, M. and Knight, J.:
702 Skilful predictions of the winter North Atlantic Oscillation one year ahead, *Nat. Geosci.*, 9, 809, 2016.

703

704 Flato, G., Marotzke, J., Abiodun, B., Braconnot, P., Chou, S. C., Collins, W., Cox, P., Driouech, F., Emori,
705 S., Eyring, V., Forest, C., Gleckler, P., Guilyardi, E., Jakob, C., Kattsov, V., Reason, C. and Rummukainen, M.:
706 IPCC 2013 AR5 - Chapter 9: Evaluation of Climate Models, *Clim. Change 2013 Phys. Sci. Basis Contrib. Work.*
707 *Group Fifth Assess. Rep. Intergov. Panel Clim. Change*, doi:10.1017/CBO9781107415324, 2013.

708

709 Fröb, F., Olsen, A., Våge, K., Moore, G. W. K., Yashayaev, I., Jeansson, E. and Rajasakaren, B.: Irminger
710 Sea deep convection injects oxygen and anthropogenic carbon to the ocean interior, *Nat. Commun.*, 7, 13244, 2016.

711

712 Good, S. A., Martin, M. J. and Rayner, N. A.: EN4: quality controlled ocean temperature and salinity
713 profiles and monthly objective analyses with uncertainty estimates, *J Geophys Res*, 118, 6704–6716, 2013.

714

715 Grist, J. P., Josey, S. a., Marsh, R., Kwon, Y. O., Bingham, R. J. and Blaker, A. T.: The surface-forced
716 overturning of the North Atlantic: Estimates from modern era atmospheric reanalysis datasets, *J. Clim.*, 27,
717 3596–3618, doi:10.1175/JCLI-D-13-00070.1, 2014.

718

719 Häkkinen, S. and Rhines, P. B.: Decline of subpolar North Atlantic circulation during the 1990s., *Science*,
720 304(2004), 555–559, doi:10.1126/science.1094917, 2004.

721

722 Hermanson, L., Eade, R., Robinson, N. H., Dunstone, N. J., Andrews, M. B., Knight, J. R., Scaife, A. A.
723 and Smith, D. M.: Forecast cooling of the Atlantic subpolar gyre and associated impacts, *Geophys. Res. Lett.*,
724 41(14), 5167–5174, doi:10.1002/2014GL060420, 2014.

725

726 Hirschi, J. J.-M., Barnier, B., Böning, C., Biastoch, A., Blaker, A. T., Coward, A., Danilov, S., Drijfhout, S.,
727 Getzlaff, K., Griffies, S. M., Hasumi, H., Hewitt, H., Iovino, D., Kawasaki, T., Kiss, A. E., Koldunov, N.,
728 Marzocchi, A., Mecking, J. V., Moat, B., Molines, J.-M., Myers, P. G., Penduff, T., Roberts, M., Treguier, A.-M.,
729 Sein, D. V., Sidorenko, D., Small, J., Spence, P., Thompson, L., Weijer, W. and Xu, X.: The Atlantic meridional
730 overturning circulation in high resolution models, *J. Geophys. Res. Oceans*, n/a(n/a), e2019JC015522,
731 doi:10.1029/2019JC015522, 2020.

732

733 Hodson, D. L. R. and Sutton, R. T.: The impact of resolution on the adjustment and decadal variability of
734 the Atlantic meridional overturning circulation in a coupled climate model, *Clim. Dyn.*, 39(12), 3057–3073,
735 doi:10.1007/s00382-012-1309-0, 2012.

736

737 Holliday, N. P., Bersch, M., Berx, B., Chafik, L., Cunningham, S., Florindo-López, C., Hátún, H., Johns,
738 W., Josey, S. A., Larsen, K. M. H., Mulet, S., Oltmanns, M., Reverdin, G., Rossby, T., Thierry, V., Valdimarsson, H.
739 and Yashayaev, I.: Ocean circulation causes the largest freshening event for 120 years in eastern subpolar North
740 Atlantic, *Nat. Commun.*, 11(1), 585, doi:10.1038/s41467-020-14474-y, 2020.

741

742 Jackson, L. C., Peterson, K. A., Roberts, C. D. and Wood, R. A.: Recent slowing of Atlantic overturning
743 circulation as a recovery from earlier strengthening, *Nat. Geosci.*, 9(7), 518–522, 2016.

744

745 Jackson, L. C., Dubois, C., Forget, G., Haines, K., Harrison, M., Iovino, D., Köhl, A., Mignac, D., Masina,
746 S., Peterson, K. A., Piecuch, C. G., Roberts, C. D., Robson, J., Storto, A., Toyoda, T., Valdivieso, M., Wilson, C.,
747 Wang, Y. and Zuo, H.: The Mean State and Variability of the North Atlantic Circulation: A Perspective From Ocean
748 Reanalyses, *J. Geophys. Res. Oceans*, 124(12), 9141–9170, doi:10.1029/2019JC015210, 2019.

749

750 Johnson, H. L., Cessi, P., Marshall, D. P., Schloesser, F. and Spall, M. A.: Recent Contributions of Theory
751 to Our Understanding of the Atlantic Meridional Overturning Circulation, *J. Geophys. Res. Oceans*, 124(8),
752 5376–5399, doi:10.1029/2019JC015330, 2019.

753

754 Josey, S. A., Hirschi, J. J.-M., Sinha, B., Ducez, A., Grist, J. P. and Marsh, R.: The Recent Atlantic Cold
755 Anomaly: Causes, Consequences, and Related Phenomena, *Annu. Rev. Mar. Sci.*, 10(1), 475–501,
756 doi:10.1146/annurev-marine-121916-063102, 2018.

757

758 Joyce, T. M., and Zhang, R.: On the Path of the Gulf Stream and the Atlantic Meridional Overturning
759 Circulation, *J. Clim.*, 23, 3146–3154, 2010.

760

761 Jungclauss, J. H., Haak, H., Latif, M. and Mikolajewicz, U.: Arctic-North Atlantic interactions and
762 multidecadal variability of the meridional overturning circulation, *J. Clim.*, 18(19), 4013–4031,
763 doi:10.1175/JCLI3462.1, 2005.

764

765 Kanzow, T., Cunningham, S. A., Johns, W. E., Hirschi, J. J.-M., Marotzke, J., Baringer, M. O., Meinen, C.
766 S., Chidichimo, M. P., Atkinson, C., Beal, L. M., Bryden, H. L. and Collins, J.: Seasonal Variability of the Atlantic
767 Meridional Overturning Circulation at 26.5°N, *J. Clim.*, 23(21), 5678–5698, doi:10.1175/2010JCLI3389.1, 2010.

768

769 Karspeck, A. R., Stammer, D., Köhl, A., Danabasoglu, G., Balmaseda, M., Smith, D. M., Fujii, Y., Zhang,
770 S., Giese, B., Tsujino, H. and Rosati, A.: Comparison of the Atlantic meridional overturning circulation between
771 1960 and 2007 in six ocean reanalysis products, *Clim. Dyn.*, Published Online-Published Online,
772 doi:10.1007/s00382-015-2787-7, 2015.

773

774 Katsman, C. A., Drijfhout, S. S., Dijkstra, H. A. and Spall, M. A.: Sinking of Dense North Atlantic Waters
775 in a Global Ocean Model: Location and Controls, *J. Geophys. Res. Oceans*, 123(5), 3563–3576,
776 doi:10.1029/2017JC013329, 2018.

777

778 Kavvada, A., Ruiz-Barradas, A. and Nigam, S.: AMO’s structure and climate footprint in observations and
779 IPCC AR5 climate simulations, *Clim. Dyn.*, 41, 1345–1364, 2013.

780

781 Kim, W. M., Yeager, S. and Danabasoglu, G.: Atlantic Multidecadal Variability and Associated Climate
782 Impacts Initiated by Ocean Thermohaline Dynamics, *J. Clim.*, 33(4), 1317–1334, doi:10.1175/JCLI-D-19-0530.1,
783 2020.

784

785 Knight, J. R., Allan, R. J., Folland, C. K., Vellinga, M. and Mann, M. E.: A signature of persistent natural
786 thermohaline circulation cycles in observed climate, *Geophys. Res. Lett.*, 32, 1–4, doi:10.1029/2005GL024233,
787 2005.

788

789 Knight, J. R., Folland, C. K. and Scaife, A. a.: Climate impacts of the Atlantic multidecadal oscillation,
790 *Geophys. Res. Lett.*, 33, 1–4, doi:10.1029/2006GL026242, 2006.

791

792 Koenigk, T. and Brodeau, L.: Arctic climate and its interaction with lower latitudes under different levels of
793 anthropogenic warming in a global coupled climate model, *Clim. Dyn.*, 49(1), 471–492,
794 doi:10.1007/s00382-016-3354-6, 2017.

795

796 Langehaug, H. R., Rhines, P. B., Eldevik, T., Mignot, J. and Lohmann, K.: Water mass transformation and
797 the North Atlantic Current in three multicentury climate model simulations, *J. Geophys. Res. Oceans*, 117(C11),
798 doi:10.1029/2012JC008021, 2012.

799

800 Li, F., Lozier, M. S., Danabasoglu, G., Holliday, N. P., Kwon, Y.-O., Romanou, A., Yeager, S. G. and
801 Zhang, R.: Local and Downstream Relationships between Labrador Sea Water Volume and North Atlantic
802 Meridional Overturning Circulation Variability, *J. Clim.*, 32(13), 3883–3898, doi:10.1175/JCLI-D-18-0735.1, 2019.

803

804 Lohmann, K., Drange, H. and Bentsen, M.: Response of the North Atlantic subpolar gyre to persistent
805 North Atlantic oscillation like forcing, *Clim. Dyn.*, 32, 273–285, doi:10.1007/s00382-008-0467-6, 2009.
806

807 Lozier, M. S., Leadbetter, S., Williams, R. G., Roussenov, V., Reed, M. S. C. and Moore, N. J.: The spatial
808 pattern and mechanisms of heat-content change in the North Atlantic., *Science*, 319, 800–803,
809 doi:10.1126/science.1146436, 2008.
810

811 Lozier, M. S., Li, F., Bacon, S., Bahr, F., Bower, A. S., Cunningham, S. A., de Jong, M. F., de Steur, L.,
812 deYoung, B., Fischer, J., Gary, S. F., Greenan, B. J. W., Holliday, N. P., Houk, A., Houpert, L., Inall, M. E., Johns,
813 W. E., Johnson, H. L., Johnson, C., Karstensen, J., Koman, G., Le Bras, I. A., Lin, X., Mackay, N., Marshall, D. P.,
814 Mercier, H., Oltmanns, M., Pickart, R. S., Ramsey, A. L., Rayner, D., Straneo, F., Thierry, V., Torres, D. J.,
815 Williams, R. G., Wilson, C., Yang, J., Yashayaev, I. and Zhao, J.: A sea change in our view of overturning in the
816 subpolar North Atlantic, *Science*, 363(6426), 516, doi:10.1126/science.aau6592, 2019.
817

818 McCarthy, G. D., Haigh, I. D., Hirschi, J. J.-M., Grist, J. P. and Smeed, D. A.: Ocean impact on decadal
819 Atlantic climate variability revealed by sea-level observations., *Nature*, 521(7553), 508–510,
820 doi:10.1038/nature14491, 2015.
821

822 Medhaug, I. and Furevik, T.: North Atlantic 20th century multidecadal variability in coupled climate
823 models: sea surface temperature and ocean overturning circulation, *Ocean Sci.*, 7, 389–404, 2011.
824

825 Menary, M. B., Hodson, D. L. R., Robson, J. I., Sutton, R. T., Wood, R. A. and Hunt, J. A.: Exploring the
826 impact of CMIP5 model biases on the simulation of North Atlantic decadal variability, *Geophys. Res. Lett.*, 42(14),
827 5926–5934, doi:10.1002/2015GL064360, 2015.
828

829 Moat, B. I., Sinha, B., Josey, S. A., Robson, J., Ortega, P., Sévellec, F., Holliday, N. P., McCarthy, G. D.,
830 New, A. L. and Hirschi, J. J.-M.: Insights into Decadal North Atlantic Sea Surface Temperature and Ocean Heat
831 Content Variability from an Eddy-Permitting Coupled Climate Model, *J. Clim.*, 32(18), 6137–6161,
832 doi:10.1175/JCLI-D-18-0709.1, 2019.
833

834 Monerie, P.-A., Robson, J., Dong, B., Dieppois, B., Pohl, B. and Dunstone, N.: Predicting the seasonal
835 evolution of southern African summer precipitation in the DePreSys3 prediction system, *Clim. Dyn.*, 52(11),
836 6491–6510, doi:10.1007/s00382-018-4526-3, 2019.
837

838 Nigam, S., Ruiz-Barradas, A., and Chafik, L.: Gulf Stream Excursions and Sectional Detachments Generate
839 the Decadal Pulses in the Atlantic Multidecadal Oscillation, *J. Clim.*, 31, 2853–2870, 2018.
840

841 Ortega, P., Hawkins, E. and Sutton, R.: Processes governing the predictability of the Atlantic meridional
842 overturning circulation in a coupled GCM, *Clim. Dyn.*, 37(9–10), doi:10.1007/s00382-011-1025-1, 2011.
843

844 Ortega, P., Mignot, J., Swingedouw, D., Sévellec, F. and Guilyardi, E.: Reconciling two alternative
845 mechanisms behind bi-decadal variability in the North Atlantic, *Prog. Oceanogr.*, 137,
846 doi:10.1016/j.pocean.2015.06.009, 2015.
847

848 Ortega, P., Robson, J., Sutton, R. T. and Andrews, M. B.: Mechanisms of decadal variability in the
849 Labrador Sea and the wider North Atlantic in a high-resolution climate model, *Clim. Dyn.*, 49(7–8),
850 doi:10.1007/s00382-016-3467-y, 2017.
851

852 Pickart, R. S. and Spall, M. a.: Impact of Labrador Sea Convection on the North Atlantic Meridional
853 Overturning Circulation, *J. Phys. Oceanogr.*, 37(1993), 2207–2227, doi:10.1175/JPO3178.1, 2007.
854

855 Piecuch, C. G., Ponte, R. M., Little, C. M., Buckley, M. W. and Fukumori, I.: Mechanisms underlying
856 recent decadal changes in subpolar North Atlantic Ocean heat content, *J. Geophys. Res. Oceans*, 122(9), 7181–7197,
857 doi:10.1002/2017JC012845, 2017.

858
859 Polo, I., Robson, J., Sutton, R. and Balmaseda, M. A.: The Importance of Wind and Buoyancy Forcing for
860 the Boundary Density Variations and the Geostrophic Component of the AMOC at 26°N, *J. Phys. Oceanogr.*, 44(9),
861 2387–2408, doi:10.1175/JPO-D-13-0264.1, 2014.

862
863 Polyakov, I.V., Alexeev, V.A., Bhatt, U.S., Polyakova, E. I., Zhang, X.: North Atlantic warming: patterns of
864 long-term trend and multidecadal variability, *Clim. Dyn.* 34, 439–457, 2010.

865
866 Rahmstorf, S., Box, J. E., Feulner, G., Mann, M. E., Robinson, A., Rutherford, S. and Schaffernicht, E. J.:
867 Exceptional twentieth-century slowdown in Atlantic Ocean overturning circulation, *Nat. Clim. Change*, 5(5),
868 475–480, doi:10.1038/nclimate2554, 2015.

869
870 Reintges, A., Martin, T., Latif, M. and Keenlyside, N. S.: Uncertainty in twenty-first century projections of
871 the Atlantic Meridional Overturning Circulation in CMIP3 and CMIP5 models, *Clim. Dyn.*, 49(5), 1495–1511,
872 doi:10.1007/s00382-016-3180-x, 2017.

873
874 Reverdin, G.: North Atlantic subpolar Gyre surface variability (1895-2009), *J. Clim.*, 23, 4571–4584,
875 doi:10.1175/2010JCLI3493.1, 2010.

876
877 Roberts, C. D., Garry, F. K. and Jackson, L. C.: A Multimodel Study of Sea Surface Temperature and
878 Subsurface Density Fingerprints of the Atlantic Meridional Overturning Circulation, *J. Clim.*, 26(22), 9155–9174,
879 doi:10.1175/JCLI-D-12-00762.1, 2013.

880
881 Roberts, M. J., Baker, A., Blockley, E. W., Calvert, D., Coward, A., Hewitt, H. T., Jackson, L. C.,
882 Kuhlbrodt, T., Mathiot, P., Roberts, C. D., Schiemann, R., Seddon, J., Vanni ere, B. and Vidale, P. L.: Description of
883 the resolution hierarchy of the global coupled HadGEM3-GC3.1 model as used in CMIP6 HighResMIP
884 experiments, *Geosci Model Dev*, 12(12), 4999–5028, doi:10.5194/gmd-12-4999-2019, 2019.

885
886 Roberts, M. J., Jackson, L. C., Roberts, C. D., Meccia, V., Docquier, D., Koenigk, T., Ortega, P.,
887 Moreno-Chamarro, E., Bellucci, A., Coward, A., Drijfhout, S., Exarchou, E., Gutjahr, O., Hewitt, H. T., Iovino, D.,
888 Lohmann, K., Schiemann, R., Seddon, J., Terray, L., Xu, X., Zhang, Q., Chang, P., Yeager, S. G., Castruccio, F.,
889 Zhang, S. and Wu, L.: Sensitivity of the Atlantic Meridional Overturning Circulation to Model Resolution in CMIP6
890 HighResMIP Simulations and Implications for Future Changes, JAMES, Published online, 2020.

891
892 Robson, J., Lohmann, K., Smith, D. and Palmer, M. D.: Causes of the rapid warming of the North Atlantic
893 Ocean in the mid-1990s, *J. Clim.*, 25(2008), 4116–4134, doi:10.1175/JCLI-D-11-00443.1, 2012.

894
895 Robson, J., Sutton, R. and Smith, D.: Predictable climate impacts of the decadal changes in the ocean in the
896 1990s, *J. Clim.*, 26, 6329–6339, doi:10.1175/JCLI-D-12-00827.1, 2013.

897
898 Robson, J., Hodson, D., Hawkins, E. and Sutton, R.: Atlantic overturning in decline?, *Nat. Geosci.*, 7(1),
899 2–3, doi:10.1038/ngeo2050, 2014.

900
901 Robson, J., Ortega, P. and Sutton, R.: A reversal of climatic trends in the North Atlantic since 2005, *Nat.*
902 *Geosci.*, 9(7), doi:10.1038/ngeo2727, 2016.

903
904 Robson, J., Polo, I., Hodson, D. L. R., Stevens, D. P. and Shaffrey, L. C.: Decadal prediction of the North
905 Atlantic subpolar gyre in the HiGEM high-resolution climate model, *Clim. Dyn.*, 50(3), 921–937,
906 doi:10.1007/s00382-017-3649-2, 2018a.

907
908 Robson, J., Sutton, R. T., Archibald, A., Cooper, F., Christensen, M., Gray, L. J., Holliday, N. P.,
909 Macintosh, C., McMillan, M., Moat, B., Russo, M., Tilling, R., Carslaw, K., Desbry eres, D., Embury, O., Feltham,
910 D. L., Grosvenor, D. P., Josey, S., King, B., Lewis, A., McCarthy, G. D., Merchant, C., New, A. L., O’Reilly, C. H.,
911 Osprey, S. M., Read, K., Scaife, A., Shepherd, A., Sinha, B., Smeed, D., Smith, D., Ridout, A., Woollings, T. and

912 Yang, M.: Recent multivariate changes in the North Atlantic climate system, with a focus on 2005–2016, *Int. J.*
913 *Climatol.*, 38(14), 5050–5076, doi:10.1002/joc.5815, 2018b.

914

915 Roussenov, V. M., Williams, R. G., Hughes, C. W. and Bingham, R. J.: Boundary wave communication of
916 bottom pressure and overturning changes for the North Atlantic, *J. Geophys. Res. Oceans*, 113(C8),
917 doi:10.1029/2007JC004501, 2008.

918

919 Schlesinger, M. E. and Ramankutty, N.: An oscillation in the global climate system of period 65-70 years,
920 *Nature*, 367(6465), 723–726, 1994.

921

922 Sgubin, G., Swingedouw, D., Drijfhout, S., Mary, Y. and Bennabi, A.: Abrupt cooling over the North
923 Atlantic in modern climate models, *Nat. Commun.*, 8 [online] Available from:
924 <http://dx.doi.org/10.1038/ncomms14375>, 2017.

925

926 Shaffrey, L., Stevens, I., Norton, W. A., Roberts, M. J., Vidale, P. L., Harle, J. D., Jrrar, A., Stevens, D. P.,
927 Woodage, M. J., Demory, M. E., Donners, J., Clark, D. B., Clayton, A., Cole, J. W., Wilson, S. S., Connolley, W. M.,
928 Davi, T. M. and Martin, G. M.: U.K. HiGEM: The New U.K. High-Resolution Global Environment Model—Model
929 Description and Basic Evaluation, *J. Clim.*, 22(8), 1861–1896, doi:10.1175/2008JCLI2508.1, 2009.

930

931 Sinha, B., Smeed, D. A., McCarthy, G., Moat, B. I., Josey, S. A., Hirschi, J. J.-M., Frajka-Williams, E.,
932 Blaker, A. T., Rayner, D. and Madec, G.: The accuracy of estimates of the overturning circulation from basin-wide
933 mooring arrays, *Prog. Oceanogr.*, 160, 101–123, doi:10.1016/j.pocean.2017.12.001, 2018.

934

935 Smeed, D. A., Josey, S. A., Beaulieu, C., Johns, W. E., Moat, B. I., Frajka-Williams, E., Rayner, D.,
936 Meinen, C. S., Baringer, M. O., Bryden, H. L. and McCarthy, G. D.: The North Atlantic Ocean Is in a State of
937 Reduced Overturning, *Geophys. Res. Lett.*, 45(3), 1527–1533, doi:10.1002/2017GL076350, 2018.

938

939 Smith, D. M. and Murphy, J. M.: An objective ocean temperature and salinity analysis using covariances
940 from a global climate model, *J. Geophys. Res. Oceans*, 112(C2), doi:10.1029/2005JC003172, 2007.

941

942 Sutton, R. T. and Hodson, D. L. R.: Atlantic Ocean forcing of North American and European summer
943 climate., *Science*, 309(2005), 115–118, doi:10.1126/science.1109496, 2005.

944

945 Sutton, R. T., McCarthy, G. D., Robson, J., Sinha, B., Archibald, A. T. and Gray, L. J.: Atlantic
946 Multidecadal Variability and the U.K. ACSIS Program, *Bull. Am. Meteorol. Soc.*, 99(2), 415–425,
947 doi:10.1175/BAMS-D-16-0266.1, 2018.

948

949 Tandon, N. F., and Kushner, P. J.: Does External Forcing Interfere with the AMOC's Influence on North
950 Atlantic Sea Surface Temperature?, *Journal of Climate*, 28, 6309-6323. 2015.

951

952 Taylor, K. E., Stouffer, R. J. and Meehl, G. A.: An Overview of CMIP5 and the Experiment Design, *Bull.*
953 *Am. Meteorol. Soc.*, 93(4), 485–498, doi:10.1175/BAMS-D-11-00094.1, 2012.

954

955 Thornalley, D. J. R., Oppo, D. W., Ortega, P., Robson, J. I., Brierley, C. M., Davis, R., Hall, I. R.,
956 Moffa-Sanchez, P., Rose, N. L., Spooner, P. T., Yashayaev, I. and Keigwin, L. D.: Anomalous weak Labrador Sea
957 convection and Atlantic overturning during the past 150 years, *Nature*, 556(7700), doi:10.1038/s41586-018-0007-4,
958 2018.

959

960 Storch, H., and Zwiers, F.: *Statistical Analysis in Climate Research*. Cambridge: Cambridge University
961 Press. doi:10.1017/CBO9780511612336, 1999.

962

963 Weijer, W., Cheng, W., Garuba, O. A., Hu, A. and Nadiga, B. T.: CMIP6 Models Predict Significant 21st
964 Century Decline of the Atlantic Meridional Overturning Circulation, *Geophys. Res. Lett.*, 47(12), e2019GL086075,
965 doi:10.1029/2019GL086075, 2020.

966
967 Woollings, T., Gregory, J., Pinto, J. G., Reyers, M. and Brayshaw, D.: Response of the North Atlantic storm
968 track to climate change shaped by ocean–atmosphere coupling, *Nat. Geosci.*, 5(5), 313–317, doi:10.1038/ngeo1438,
969 2012.
970
971 Xu, X., Chassignet, E. P. and Wang, F.: On the variability of the Atlantic meridional overturning circulation
972 transports in coupled CMIP5 simulations, *Clim. Dyn.*, 52(11), 6511–6531, doi:10.1007/s00382-018-4529-0, 2019.
973
974 Yan, X., Zhang, R. and Knutson, T. R.: Underestimated AMOC Variability and Implications for AMV and
975 Predictability in CMIP Models, *Geophys. Res. Lett.*, 45(9), 4319–4328, doi:10.1029/2018GL077378, 2018.
976
977 Yashayaev, I. and Loder, J. W.: Recurrent replenishment of Labrador Sea Water and associated
978 decadal-scale variability, *J. Geophys. Res. Oceans*, 121, 8095–8114, doi:10.1002/2016JC012046, 2016.
979
980 Yeager, S.: Topographic Coupling of the Atlantic Overturning and Gyre Circulations, *J. Phys. Oceanogr.*,
981 45(5), 1258–1284, doi:10.1175/JPO-D-14-0100.1, 2015.
982
983 Yeager, S. and Danabasoglu, G.: The Origins of Late-Twentieth-Century Variations in the Large-Scale
984 North Atlantic Circulation, *J. Clim.*, 27(9), 3222–3247, doi:10.1175/JCLI-D-13-00125.1, 2014.
985
986 Yeager, S. G. and Robson, J. I.: Recent Progress in Understanding and Predicting Atlantic Decadal Climate
987 Variability, *Curr. Clim. Change Rep.*, 3(2), 112–127, doi:10.1007/s40641-017-0064-z, 2017.
988
989 Zhang, L. and Wang, C.: Multidecadal North Atlantic sea surface temperature and Atlantic meridional
990 overturning circulation variability in CMIP5 historical simulations, *J. Geophys. Res. Oceans*, 118(10), 5772–5791,
991 doi:10.1002/jgrc.20390, 2013.
992
993 Zhang, R.: Coherent surface-subsurface fingerprint of the Atlantic meridional overturning circulation,
994 *Geophys. Res. Lett.*, 35, 1–6, doi:10.1029/2008GL035463, 2008.
995
996 Zhang, R. and Delworth, T. L.: Impact of Atlantic multidecadal oscillations on India/Sahel rainfall and
997 Atlantic hurricanes, *Geophys. Res. Lett.*, 33(17), doi:10.1029/2006GL026267, 2006.
998
999 Zhang, R., Delworth, T. L., Rosati, A., Anderson, W. G., Dixon, K. W., Lee, H. C. and Zeng, F.: Sensitivity
1000 of the North Atlantic Ocean Circulation to an abrupt change in the Nordic Sea overflow in a high resolution global
1001 coupled climate model, *J. Geophys. Res. Oceans*, 116, 1–14, doi:10.1029/2011JC007240, 2011.
1002
1003 Zhao, J. and Johns, W.: Wind-forced interannual variability of the Atlantic Meridional Overturning
1004 Circulation at 26.5 N, *J. Geophys. Res. Oceans*, 2403–2419, doi:10.1002/2013JC009407.Received, 2014.
1005
1006 Zou, S., Lozier, M. S. and Xu, X.: Latitudinal Structure of the Meridional Overturning Circulation
1007 Variability on Interannual to Decadal Time Scales in the North Atlantic Ocean, *J. Clim.*, 33(9), 3845–3862,
1008 doi:10.1175/JCLI-D-19-0215.1, 2020.
1009